Progress in Oceanography 197 (2021) 102642

Contents lists available at ScienceDirect

Progress in Oceanography

journal homepage: www.elsevier.com/locate/pocean

On the extreme value statistics of spatio-temporal maximum sea waves under cyclone winds

Alvise Benetazzo [a,*], Francesco Barbariol [a], Filippo Bergamasco [b], Luciana Bertotti [a], Jeseon Yoo [c], Jae-Seol Shim [c], Luigi Cavaleri [a]

[a] Istituto di Scienze Marine (ISMAR), Consiglio Nazionale delle Ricerche (CNR), 30122 Venice, Italy
[b] DAIS – Università Ca' Foscari, Venice, Italy
[c] Korea Institute of Ocean Science and Technology (KIOST), 49111 Pusan, Republic of Korea

ARTICLE INFO

Keywords:
Maximum waves
Spatio-temporal extreme value statistics
Tropical storm
Northwestern Pacific
Kong-rey (2018)
Spectral wave models
Bimodal sea states
Stereo wave imaging

ABSTRACT

Principles of the spatio-temporal statistics are used to investigate the characteristics of short-term/range extreme sea waves and related sea-state parameters under cyclone winds (northern hemisphere). We base our analysis upon consistent stereo-imaging observations of the 3D (2D space + time) sea surface elevation field, and spectral wave model results in the Northwestern Pacific during tropical storm Kong-rey (2018). The focus is on the extreme value analysis of individual maximum sea surface elevations (crest heights) and maximum crest-to-trough wave heights. Results highlight the sea areas around the storm centre where the spatio-temporal highest waves are more likely, and, via scale analysis, the principal mechanisms responsible for the occurrence of extreme conditions in bimodal (composed of wind-sea and swell) and short-crested storm seas. We find that individual waves are the highest to the north-east of the translating cyclone, where sea states are more energetic. However, in the south/south-west of the centre, where opposing wind-sea/swell sea states dominate, directional spread and bound nonlinear interactions are enhanced. In this area, more extreme waves may occur, having the maximum crest and wave heights mean values in excess of 1.3 and 2.1 times the significant wave height, respectively. This set of results provides insights into the role of the dispersive and directional focusing enhanced by nonlinearities up to the second order as an effective mechanism for the formation of extreme waves under cyclone winds. To examine what physical mechanism is behind the generation of extreme waves in different regions around the cyclone, we also explore for comparison areas where nonlinear four-wave interactions are more likely to occur.

1. Introduction

Atmospheric storms produce violent winds that force severe sea states, which are the primary cause of severe disasters such as coastal floods, ship accidents, and damages to offshore platforms and coastal structures. One of the sources of such conditions is the tropical cyclones, which are rapidly rotating storm systems characterized by a deep low-pressure centre. In the Northwestern Pacific basin, typhoons and tropical storms are some of the disastrous extreme weather events, causing storm surges with extremely large waves and other destructive impacts along the coasts (Fu et al., 2016; Liu et al., 2009; Wada et al., 2014). In recent years, strong typhoons have been observed with record-breaking waves, such as Kompasu (#1007), Bolaven (#1215) and Sanba (#1216). For instance, Sanba made landfall on the south of the Korean peninsula with peak significant wave heights of 13.4 m measured on the coast and about 16 m hindcasted in the East China Sea (Moon et al., 2016). One or two typhoons per year occur on average in the East China Sea and Yellow Sea (Li et al., 2020; Yu et al., 2020). They tend to be intensified by passing over the area due to regional enforcements such as increased travel speeds by prevailing westerlies and high-temperature seawater. This intensification of typhoons over the area leads to severe coastal disasters by extreme wave events in the Yellow Sea and the southern coast of Korea, causing economic losses in the order of tens of million US dollars per year (Jun et al., 2015; Wang et al., 2020).

Over the global oceans, the characterization of extreme wave events during storms has been an active topic of research for decades because of its importance for marine safety, coastal hazards, offshore design and operations. Significant and valuable efforts have been conducted to

* Corresponding author.
E-mail address: alvise.benetazzo@ismar.cnr.it (A. Benetazzo).

https://doi.org/10.1016/j.pocean.2021.102642
Received 29 March 2021; Received in revised form 25 June 2021; Accepted 13 July 2021
Available online 23 July 2021

understand the likelihood of extreme events, up to the rogue-wave scale (Benetazzo et al., 2017a; Cavaleri et al., 2016, 2012; Dematteis et al., 2019; Donelan and Magnusson, 2017; Dysthe et al., 2008; Fedele et al., 2017; Gemmrich and Garrett, 2011; Janssen et al., 2003; Onorato et al., 2001, 2013; Slunyaev et al., 2005; Toffoli et al., 2005; Waseda et al., 2011). However, current strategies and forecast capabilities sometimes resulted ineffective in warning seafarers and avoiding structural damage to offshore and coastal facilities (Bitner-Gregersen and Gramstad, 2015; Didenkulova, 2020; Fedele et al., 2017; Mao et al., 2016). In this respect, the characteristics of wind-generated ocean waves under cyclonic storms have been studied extensively with comprehensive understanding (e.g., Liu et al., 2017; Moon et al., 2003; Young, 2017, 1988); this knowledge is not plainly applicable, however, with regard to the formation of individual, extreme waves in these conditions, a process that remains not totally understood. Past observations (Guedes Soares et al., 2004; Santo et al., 2013; Wang, 2005) and spectral wave modelling results (Jiang et al., 2019; McAllister et al., 2019; Mori, 2012) seem to suggest that competing mechanisms may explain the occurrence of single high waves, even exceeding the rogue wave threshold. The question to be addressed is the role of interacting multiple wave systems (i.e., a combination of wind-sea and remotely generated swell, produced by the rapidly varying, spiralling cyclone winds) in enhancing or reducing the probability of encountering high waves.

It is a general feature of translating cyclone winds that the ocean wave directional spectrum's resulting shape and the related bulk parameters vary noticeably around the storm centre. In particular, the maximum significant wave height in such storms can be represented using an extended fetch model (King and Shemdin, 1978; Young, 2017), whose effect is such that the degree of asymmetry of the wind field (stronger winds to the right in the northern hemisphere) is far smaller than the wave field. For the latter, the characterization of Black et al. (2007) distinguished in the geographical space three azimuthal sectors experiencing different types of mixed sea states, with swells and locally generated wind seas travelling in many directions and producing a uni or bimodal shape of the spectra. The work by Holthuijsen et al. (2012) highlighted the swell types in a hypothetical hurricane and the following (angle between the wind and swell $< 45°$), cross (angle between 45° and 135°), and opposing (angle $> 135°$) conditions for the swell and the wind sea (see also Hu and Chen, 2011, and Liu et al., 2017). As a result, the resulting sea states produce characteristic patterns for the wave spectrum parameters and surface roughness.

As for the extreme wave generation in general environments, early researches discussed it in the context of nonlinear instability of deep-water waves (Janssen et al., 2003; Mori and Janssen, 2006; Waseda et al., 2011). In nonlinear models that allow for energy focusing due to modulation instability (Benjamin and Feir, 1967), the interaction of two plane-wave systems with different direction of propagation was reported as a possible mechanism for extreme wave formation in deep water (Onorato et al., 2010). However, in the framework of a system of two coupled nonlinear Schrödinger equations (Zakharov, 1968), the crossing angle must be kept smaller than about 60° to 70° (Cavaleri et al., 2012) since, for larger angles, the solution of equations becomes of defocusing type. Indeed, nonlinear Schrödinger type modulational instabilities attenuate as the wave spectrum broadens (Onorato et al., 2009), such that their role in the generation of extreme stormy waves was questioned (see, e.g., Fedele et al., 2016). On the other hand, the constructive interference of 3D elementary waves with random amplitudes and phases enhanced by second-order bound nonlinearities has been proposed as an effective mechanism for extreme and rogue wave generation (Benetazzo et al., 2015; Fedele, 2012). The impact of multiple systems on spatio-temporal maximum wave elevations was firstly analyzed by Baxevani and Rychlik (2004). They proposed that counter-propagating, short-crested (i.e., laterally spread), and uncorrelated sea states with random phases maximize, in Gaussian seas, the likelihood of very high surface elevations.

Under typhoon winds, the study by Mori (2012) suggested that long-crested, uni-directional extreme waves resulting from nonlinear instability have a great potential of occurring in the south-east of the storm centre (northern hemisphere), where waves are steep and have narrow frequencies and directional spectra. It is also suggested that in the south and west areas around the storm centre, the large directional spread (resulting from the combination of wind-sea and swell) attenuates the nonlinear four-wave interactions, and the wave field is weakly nonlinear. In that study, at the same time, the role of directionality is not considered as a potential mechanism for the enhancement of the surface elevation. However, as pointed out above, other research indicates that spatio-temporal maxima of short-crested, multi-directional wave trains are enhanced if the energy can spread laterally. This debate provides our principal motivation for studying how the extreme wave generation proceeds under the forcing of multiple wave systems that may maximize the width (frequency and directions) of the resulting sea state. The focus will be on the wave extremes at short term/range by considering the role of the 3D (2D space + time) geometry of the wave field.

Following the summary mentioned above, the present paper will examine the spatio-temporal statistics of maximum waves (crest and crest-to-trough heights) in the Northwestern Pacific under realistic cyclone winds associated with the tropical storm Kong-rey (2018). In situ observations using a stereo wave imaging system and spectral wave model results (from the European Centre for Medium-Range Weather Forecasts, ECMWF) will be used. They allowed us to discuss in detail the cyclone regions where the highest waves are more likely to occur, resulting from dispersive and directional focusing of elementary wave harmonics enhanced by second-order nonlinear effects. The assessment of model directional spectrum estimations (of wave maxima, steepness, frequency and direction widths, significant wave height) with observed wave data will also be discussed.

The arrangement of the paper is as follows. Section 2 introduces the relevant information on the Kong-rey storm, and the basic extreme-value statistical principles used in this paper. Details pertaining to the 3D wave field observation, the wind and spectral wave models are also incorporated in this section. Section 3 is dedicated to comparing model and measurements, and it provides the principal results regarding the geographical pattern of maximum waves and related sea parameters around the storm centre. A discussion and summary of the main conclusions of the study are presented in section 4.

2. Material and methods

2.1. The tropical storm Kong-rey (2018)

The northern hemisphere tropical storm Kong-rey (#1825) developed in late September 2018 as a large and powerful typhoon that was tied with Typhoon Yutu as the most powerful tropical cyclone worldwide in 2018. The twenty-fifth tropical storm, eleventh typhoon and 6th super-typhoon of the 2018 Pacific typhoon season, Kong-rey originated from a tropical disturbance in the open Pacific Ocean; for a couple of days, it went westward, organizing into a tropical depression on 27 September. Then, it intensified into a powerful Category five super-typhoon early on 2 October. Kong-rey underwent an eyewall replacement cycle after its peak intensity, causing it to weaken into a Category 3 typhoon under unfavourable conditions. Increased vertical wind shear and lower sea surface temperatures hampered Kong-rey's strength, and it downgraded to a tropical storm on 4 October. Early on 6 October, Kong-rey made landfall with 975 hPa central pressure in Tongyeong, South Kyongsang Province in South Korea as a high-end tropical storm, and later on the same day, Kong-rey transitioned into an extra-tropical cyclone, while impacting southern Hokkaido (Japan), such as areas near Hakodate. Detailed information on the strength and the track of Kong-rey can be found at https://blogs.nasa.gov/hurricanes/tag/kong-rey-2018/ and http://agora.ex.nii.ac.jp/digital-typhoon/summary/wnp/s/201825.html.en (latest visits on 25 June 2021).

2.2. Extreme value statistics of spatio-temporal maximum waves

2.2.1. General principles

In this section, we shall summarize the principal physical mechanisms and theoretical models used to describe the extreme-value statistics of the maximum waves sustained by the winds during Kong-rey. Let the spatio-temporal sea surface elevation field, with zero-mean and standard deviation σ, be $\eta(x, y, t) = \eta(\boldsymbol{x}, t)$, where $\boldsymbol{x} = (x, y)$ denotes the horizontal coordinate vector, and t denotes time. For a given sea state of significant wave height $H_s = 4\sigma$, the variables of interest are (*i*) the maximum individual crest-to-trough wave height H_{max} and (*ii*) the maximum sea surface elevation (i.e., the individual maximum crest height) C_{max}. We refer, in particular, to the spatio-temporal statistics at a short-term/range (interval $\sim$ 1 h and extent in deep water $\sim$ 1 km), by incorporating, in the sea state characterization, the requirements of stationarity and homogeneity (Holthuijsen, 2007; Ochi, 1998). The domain of interest spans time and the 2D sea surface space, and the statistics of short-crested maximum waves belonging to wave trains propagating across a finite surface region is investigated (Fedele, 2012; Krogstad et al., 2004) by stemming on the analyses made for multi-dimensional manifolds (Adler, 1981; Piterbarg, 1996). For the variables H_{max} and C_{max}, we discuss below the principal parameters used for the description of the statistics and their means to isolate the meaningful processes responsible for the theoretical occurrence of large values. From the complete statistics, we shall consider the expectations of the two heights, which we indicate with an overbar as $\overline{H}_{max}$ and $\overline{C}_{max}$.

The theoretical model approximating the occurrence probability of individual wave crests C is posed in the form of a second-order nonlinear solution (Longuet-Higgins, 1963; Tayfun, 1980), and the *steepness* parameter is used for its characterization, being it closely associated with the positive skewness of the nonlinear sea surface elevation (Fedele and Tayfun, 2009). We then rely on the constructive interference, at a short interaction scale, of 3D elementary, focusing waves with random amplitudes and phases enhanced by second-order bound (non-resonant) nonlinearities as the leading mechanism for the statistics of spatio-temporal maximum surface elevations (Benetazzo et al., 2015). Since higher-order harmonics may increase rapidly when the wave group focuses, a further approximation that includes third-order nonlinearities was developed by Fedele et al. (2017). However, those authors demonstrated that second-order nonlinearities are dominant during the formation of realistic, laterally spread focused waves, with a negligible effect of third-order nonlinear interactions, in agreement with recent studies on rogue wave probabilities (Fedele et al., 2016). The third-order solution will be assessed later in this study in the comparison between numerical predictions and observations. For the individual wave heights (crest-to-trough vertical distance H), we shall adopt a model based on a Rayleigh-like distribution function (Longuet-Higgins, 1952) with a scale parameter that is characterized for a finite *bandwidth* of the wave spectrum, assuming that both the crest height and the trough depth are random variables (Boccotti, 2000; Casas-Prat and Holthuijsen, 2010; Naess, 1985). The theory establishes that the average profile of high waves in a random sea is represented by a suitably scaled focussed wave group with a shape proportional to the autocorrelation function of the underlying random process. We remark that the statistical models here adopted are consistent with the recent marine structure guidelines for modelling, analysis and prediction of metocean design and operational conditions (DNV GL, 2017). Moreover, these model fit the extreme-wave implementations in state-of-the-art spectral wave models, such as WAVEWATCH III® and WAM (Barbariol et al., 2017; Benetazzo et al., 2021).

As for the extreme values of H and C, following Gumbel (1958), the statistics of the random variables H_{max} and C_{max} is written as a function of the initial probability distribution and of the *sample size* (i.e., the average number of waves in a given domain). Accordingly, the functional forms of $\overline{C}_{max}$ and of $\overline{H}_{max}$ can be written as follows:

$$\overline{C}_{max} = H_s\, f_{Cmax}(steepness,\ \ sample\ \ size) \tag{1}$$

$$\overline{H}_{max} = H_s\, f_{Hmax}(bandwidth,\ \ sample\ \ size) \tag{2}$$

where H_s represents the severity of sea condition. Without loss of generality, the two functions monotonically increase for increasing *sample size*, f_{Cmax} increases for steep sea states, while f_{Hmax} provides larger wave heights for narrow wave trains.

In this study, the two nonlinear functions f_{Cmax} and f_{Hmax} are defined for spatio-temporal extremes and are characterized as in Benetazzo et al. (2017b) (their Eq. (17) for $\overline{H}_{max}$ and Eq. 30 for $\overline{C}_{max}$ have been adopted herein; see our section 2.2.5 for details), to account for the 3D geometry of short-crested storm waves (Baxevani and Rychlik, 2004; Benetazzo et al., 2015; Fedele, 2012; Fedele et al., 2013, 2012; Krogstad et al., 2004; Magnusson et al., 1999). Our choice was dictated by the fact that spatio-temporal extreme values proved to be valuable in describing the amplitude and probability of wave and crest heights of large wave groups irrespective of any bandwidth or directional constraint (Barbariol et al., 2019; Benetazzo et al., 2021, 2018a, 2015; Cavaleri et al., 2017; Fedele et al., 2013, 2012; Mendes and Scotti, 2020). This property is convenient for describing the large variety of sea states that develop under spiralling winds.

We point out that H_s is the principal vertical scale of extreme heights, while other parameters have a relatively minor effect on the statistics of H_{max} and C_{max}. In other words, at the leading order, the larger H_s, the larger $\overline{C}_{max}$ and $\overline{H}_{max}$, regardless of the different characteristics of the sea state. Indeed, f_{Cmax} may take typical values in the range [1.1, 1.5] and f_{Hmax} in the range [1.7, 2.4] (Benetazzo et al., 2020), while H_s may vary by more than one order of magnitude over the global oceans. In terms of spectral wave model estimates (Gelci et al., 1957), this implies that the total energy would rule the prediction of maxima, and it can eventually mask the contribution of other forcings that may change the geometry of the wave field. This argument was adopted in the study by Mori and Janssen (2006), where the dependence on the *sample size* and on the kurtosis parameter of the averaged maximum envelope height was shown after normalization with H_s, which is, at the same time, the appropriate way to represent the frequency of occurrence of rogue waves (Draper, 1964; Dysthe et al., 2008; Onorato et al., 2013).

2.2.2. 3D (2D space + time) sample size and geometry

As anticipated, the general formulations of extremes given by f_{Cmax} and f_{Hmax} depend on the *sample size* plus, on the one hand, the *steepness* and, on the other hand, the *bandwidth*. Before proceeding to isolate their specific contributions, it is worth discussing the meaning of these variables. In the context of spatio-temporal extremes, the *sample size* is composed of three terms (Baxevani and Rychlik, 2004; Fedele, 2012): (*i*) the average number N_{3D} of 3D waves over the spatio-temporal domain $\Gamma \in \Re^3$, (*ii*) the average number N_{2D} of 2D waves on the lateral faces ($\Re^2$) of Γ, and (*iii*) the average number N_{1D} of 1D waves on the boundaries ($\Re^1$) of Γ. The first term (*i*) provides most of the contribution to the values of the total *sample size* for a relatively large size V of Γ (Fedele et al., 2012), and it is the only one discussed in this study. It takes the following formulation:

$$sample\ \ size = N_{3D} = \frac{XYD}{L_x L_y T_z}\sqrt{1 - \alpha_{xt}^2 - \alpha_{xy}^2 - \alpha_{yt}^2 + 2\alpha_{xt}\alpha_{xy}\alpha_{yt}} \tag{3}$$

where X and Y are the orthogonal sides of the sea surface 2D region where maxima are sought over the time interval of duration D. The 2D spatial and 1D temporal parallelepiped Γ is therefore defined with sides $[0, X] \times [0, Y] \times [0, D]$ and takes the finite size $V = XYD$. The characteristic lengths of the sea state in Eq. (3) are the mean wavelength L_x (evaluated along the peak wave direction) and, orthogonal to it, the mean crest length L_y, while T_z is the zero-crossing average period. The product $L_x L_y$ is the mean wave size in the two-dimensional spatial domain.

The operator with the square root in Eq. (3) expressed as

$$A = \sqrt{1 - \alpha_{xt}^2 - \alpha_{xy}^2 - \alpha_{yt}^2 + 2\alpha_{xt}\alpha_{xy}\alpha_{yt}} \tag{4}$$

represents the degree of organization of the spatio-temporal wave field, and it indicates how many fewer 3D exceedances should someone expect due to the organized wave motion. The variable A stems from the determinant of the 3x3 covariance matrix Λ of the surface elevation 3D gradient vector (Adler, 2000), which is defined as follows:

$$\Lambda = \begin{bmatrix} <\eta_x\eta_x> & <\eta_x\eta_y> & <\eta_x\eta_t> \\ <\eta_y\eta_x> & <\eta_y\eta_y> & <\eta_y\eta_t> \\ <\eta_t\eta_x> & <\eta_t\eta_y> & <\eta_t\eta_t> \end{bmatrix} \tag{5}$$

The spatio-temporal gradient vector is given by

$$\nabla\eta = (\eta_x, \eta_y, \eta_t) = \left(\frac{\partial\eta}{\partial x}, \frac{\partial\eta}{\partial y}, \frac{\partial\eta}{\partial t}\right) \tag{6}$$

The three terms η_x, η_y, and η_t represent the first-order partial derivatives of η with respect to the x-, y-, and t-coordinate, respectively. Using the random-phase/amplitude model (Pierson et al., 1955), the minors and determinant of Λ can be obtained analytically from the spectral moments as follows (Fedele, 2012):

$$\det(\Lambda) = m_{200}m_{020}m_{002}\left(1 - \alpha_{xt}^2 - \alpha_{xy}^2 - \alpha_{yt}^2 + 2\alpha_{xt}\alpha_{xy}\alpha_{yt}\right) \tag{7}$$

where

$$\alpha_{xt} = \frac{m_{101}}{\sqrt{m_{200}m_{002}}},\ \alpha_{yt} = \frac{m_{011}}{\sqrt{m_{020}m_{002}}},\ \alpha_{xy} = \frac{m_{110}}{\sqrt{m_{200}m_{020}}} \tag{8}$$

and m_{abc} are the moments of the directional wave spectrum $S(\omega, \theta)$, which are given by

$$m_{abc} = \iint k_x^a k_y^b \omega^c S(\omega,\theta)\mathrm{d}\omega\mathrm{d}\theta \tag{9}$$

with $\omega = 2\pi f$ the angular frequency, θ the wave direction (in this study, the flow direction is used), and (k_x, k_y) the components of the wavenumber vector $\boldsymbol{k}$.

Coefficients $\alpha = \{\alpha_{xt}, \alpha_{yt}, \alpha_{xy}\}$ in Eq. (8) convey the irregularity parameters of the 3D sea state taking values in [-1, +1] (Baxevani and Rychlik, 2004) since they are equal to the normalized cross-correlation coefficient between the components of $\nabla\eta$, i.e.,

$$\alpha_{xt} = \frac{<\eta_x\eta_t>}{\sqrt{<\eta_x^2><\eta_t^2>}},\ \alpha_{yt} = \frac{<\eta_y\eta_t>}{\sqrt{<\eta_y^2><\eta_t^2>}},\ \alpha_{xy} = \frac{<\eta_x\eta_y>}{\sqrt{<\eta_x^2><\eta_y^2>}} \tag{10}$$

In particular, the value of $\det(\Lambda)$ provides a measure of the differential entropy of the distribution: the larger the determinant, the more the data points are dispersed in space and time. An interpretation of the above coefficients was given in the Baxevani and Rychlik's study (2004), which points out their values for characteristic uni and bimodal spectral distributions. In particular, focusing on the xt and yt coefficients, they take the values $(\alpha_{xt}, \alpha_{yt}) = (0.89, 0)$ for a unimodal sea state with a JONSWAP frequency spectrum (Hasselmann et al., 1973) with $\cos^2$ symmetric directional distribution and peak direction along the x-axis (i.e., there is no organized motion along the y-axis, and therefore $\alpha_{yt} = 0$). If the sea state is composed of two independent wave modes crossing at an angle of 90°, then $(\alpha_{xt}, \alpha_{yt}) = (0.51, 0.51)$. Further, if the two modes have opposing peak directions (separation of 180°) along the x- or y-axis, then $(\alpha_{xt}, \alpha_{yt}) = (0, 0)$. In other words, the three coefficients $\{\alpha_{xt}, \alpha_{yt}, \alpha_{xy}\}$ may be interpreted as marginal spectral width parameters describing the spatio-temporal geometry of the wave field. Overall, they provide, through the variable A, a measure of the 3D width of the wavenumber/frequency spectrum. It follows that

- $A \to 1$ for a broad, multimodal sea ($\alpha \to 0$), which therefore maximizes the 3D *sample size* N_{3D}.
- $A \to 0$ for a narrow, unimodal sea ($\alpha \to 1$), for which data points do not occupy the whole 3D space (and the 3D *sample size* is practically null).

Therefore, the set of coefficients α, the variable A, and the determinant $\det(\Lambda)$ seem appropriate to investigate the statistics of extreme waves under cyclone winds since these are generally composed of bimodal, mixed swell and wind-sea crossing at different angles (Holthuijsen et al., 2012).

To summarize, in the context of spatio-temporal wave extremes that are dominated by constructive interference, the distributions of the maximum crest and wave heights depend upon the 3D width of the wave field, being them larger when the sea state is broad in direction. The validity of such a conclusion and its limitations will be discussed later in this paper when theoretical expectations will be assessed against observations and used to estimate the maximum wave fields under the cyclone. For the time being, we only note that the here adopted 3D spatio-temporal approach differs from and complements other ones used in previous studies, which investigated in a time extreme framework (i.e., 1D *sample size*) the rogue wave probability under cyclone wind conditions (Mori, 2012; Ponce de León and Guedes Soares, 2014). In those studies, nonlinear and narrow-banded spectrum waves were favoured by following the theory of Mori and Janssen (2006), which accounts for the kurtosis parameter as an indicator of the nonlinear wave interactions. A comparison between the two approaches is provided later in this study.

2.2.3. The domain of extremes

In the following, the extreme value analysis will be performed by adopting two different strategies for the characterization of the 3D *sample size*. Firstly, the spatio-temporal maximum waves during the tropical storm are determined by considering the value of $\overline{H}_{\max}$ and $\overline{C}_{\max}$ over a domain Γ of fixed size V (i.e., X, Y, D = constant) to give an overview of the geographical pattern and intensity of the two heights during Kong-rey. Secondly, we consider a sea state dependent, variable-size domain, with sides $X \sim L_x$, $Y \sim L_y$, and $D \sim T_z$. The latter approach removes the dependence of N_{3D} on L_x, L_y, and T_z, makes $f_{\mathrm{Cmax}} = f_{\mathrm{Cmax}}(A,$ *steepness*) and $f_{\mathrm{Hmax}} = f_{\mathrm{Hmax}}(A,$ *bandwidth*), and therefore it permits to highlight the sea regions where the role of the 3D wave geometry, *steepness*, and *bandwidth* may be dominant in producing more extreme conditions. We note that the use of a variable domain of extremes is required to prevent that the normalized extremes $\overline{H}_{\max}/H_s$ and $\overline{C}_{\max}/H_s$ reach the highest values in sea regions where young and short waves dominate and, as a consequence, the *sample size* (either 1D or 3D) is maximized (Ponce de León and Guedes Soares, 2014).

2.2.4. Wave steepness and bandwidth parameter

The contribution of second-order bound-wave nonlinearities in the characterization of $\overline{C}_{\max}$ is conveyed by the characteristic wave *steepness* μ. Drawing on Fedele and Tayfun (2009), a convenient formula of μ for deep-water waves is as follows:

$$\mu = \frac{\sigma\omega_1^2}{g}(1 - \upsilon + \upsilon^2) \tag{11}$$

where ω_1 is the average angular frequency and ν is the Longuet-Higgins (1975) width of the 1D frequency spectrum given by

$$\upsilon = \sqrt{m_{002}m_{000}/m_{001}^2 - 1} \tag{12}$$

Like the parameter A, ν tends to zero for a very narrow spectrum, but it brings information on the temporal shape only since it depends on the

time derivative $\frac{\partial \eta}{\partial t}$. A modification of Eq. (11), which is valid for narrow-band long-crested waves in transitional depths, was proposed by Tayfun (2006); its practical use will be discussed later with regard to wave data (model and observations) at the Gageocho Ocean Research Station in the South Yellow Sea.

As for the distribution function of $H_{\max}$, we rely on the Boccotti (2000) asymptotic formula that gives to the modified Rayleigh parameter the meaning of 1D *bandwidth*. This is approximated by the normalized minimum $\psi^* \in [-1, 0)$ of the autocovariance function $\psi(\tau)$ of the elevation time series $\eta(t)$, that is,

$$\psi^* = \min\{\psi(\tau)\}/\max\{\psi(\tau)\} \tag{13}$$

The autocovariance function can be expressed through spectral integral as follows:

$$\psi(\tau) = \int_{\omega}\int_{\theta} S(\omega,\theta)\cos(\omega\tau)\mathrm{d}\omega\mathrm{d}\theta \tag{14}$$

Drawing on the theory of quasi-determinism (Boccotti, 2000; Lindgren, 1972), typical values of $|\psi^*|$ are in the range [0.65, 0.75] for sea states with a unimodal dominant component. If $|\psi^*|$ falls below about 0.6, the sea state is most likely composed of wind waves superimposed on a swell with similar energy but different dominant frequencies. Indeed, the simultaneous presence of wind and swell waves leads to a broader, bimodal frequency spectrum, and consequently to a smaller value of $|\psi^*|$. Since the extreme value $\overline{H}_{\max}$ scales with $|\psi^*|$ through the quasi-deterministic factor

$$f_{\psi}(\psi^*) = \sqrt{2(1+|\psi^*|)} \le 2 \tag{15}$$

mixed (and generally broad-banded) sea conditions are responsible for crest-to-trough wave heights smaller than those in narrowband sea states, which maximise the correlation between the crest height and the trough depth of a wave (the upper limit is for the Rayleigh distribution that scales with $|\psi^*| = 1$ and hence $f_{\psi} = 2$).

2.2.5. Spatio-temporal maximum wave and crest heights

The theoretical formulae used in this study to estimate the maximum wave and crest heights are here reported stemming from Benetazzo et al. (2017b) results. For large elevations of the 3D wave field $\eta(x, y, t)$, the expected value of the maximum crest height over the spatio-temporal domain Γ is defined as follows:

$$\overline{C}_{\max} = \left(\xi_0 + \frac{\mu}{2}\frac{\xi_0^2}{\sigma}\right) + \sigma\gamma\left[\left(1+\mu\xi_0\sigma^{-1}\right)\times\left(\xi_0\sigma^{-1} - \frac{2N_3\xi_0\sigma^{-1}+N_2}{N_3\xi_0^2\sigma^{-2}+N_2\xi_0\sigma^{-1}+N_1}\right)^{-1}\right] \tag{16}$$

where $\xi_0\sigma^{-1}$ is the mode of the probability density function (pdf) of linear space–time extremes (Fedele et al., 2012), $N_3 = 2\pi N_{3D}$, $N_2 = \sqrt{2\pi}N_{2D}$, $N_1 = N_{1D}$, and $\gamma \approx 0.5772$ is the Euler-Mascheroni constant. As for the maximum wave heights, the expected value is given by the following expression

$$\overline{H}_{\max} = \left[\xi_0 + \sigma\gamma\left(\xi_0\sigma^{-1} - \frac{2N_3\xi_0\sigma^{-1}+N_2}{N_3\xi_0^2\sigma^{-2}+N_2\xi_0\sigma^{-1}+N_1}\right)^{-1}\right] \times\sqrt{2(1+|\psi^*|)} \tag{17}$$

2.3. Field data

Within this study, in-situ observations in the Yellow Sea during the cyclone Kong-rey have been considered to characterize the metocean conditions and to assess wave and wind model results. For these purposes, the data were collected from the fixed offshore platform Gageocho Ocean Research Station (hereinafter GORS; Fig. 1), which is located 150 km east of the southern edge of Korea and on an average depth d of 33 m. The station is built on a small, submerged ridge, rising from an almost flat bottom, with variable depth from 90 m to 30 m and an extent of about 1.5 km × 1.5 km.

For the sea state and extreme wave characterizations during the tropical storm Kong-rey, field data of the spatio-temporal sea surface elevation field $\eta(x, y, t)$ were recorded from GORS using two stereo cameras (Fig. 2) designed on the basis of the Wave Acquisition Stereo System (WASS) technology (Benetazzo, 2006; Benetazzo et al., 2012) and software (Bergamasco et al., 2017). On GORS, WASS was mounted facing east at + 26.5 m above the mean sea level, and it had a setup identical to that described in a previous study that focused on sea states at the further north Socheongcho Ocean Research Station (Benetazzo et al., 2018a). The stereo processing's primary result was a temporal sequence (at 7.5 Hz frame rate) of sea surface elevation fields $\eta(x, y)$. Due to the adopted cameras setup and setting, we expect that errors in sea surface vertical displacement η have a maximum absolute value of about 0.1 m and a root-mean-square error of 0.03 m. For processing purposes, 3D scatter points $\eta(x, y)$ were bi-linearly interpolated onto an Earth-referenced xy-grid with uniform spacing of 0.5 m, spanning the rectangular region $x \in$ [-70 m, 70 m] and $y \in$ [40 m, 160 m]. To limit the influence of high-frequency noise, independent time series $\eta(t)$ taken at each xy-position of the gridded elevation were low-pass filtered at 0.9 Hz. This frequency range also allows a better consistency with the estimations of sea state parameters from model spectra.

Using the stereo cameras, eight 20-minute-long bursts were considered on 5 and 6 October 2018, when Kong-rey moved north towards

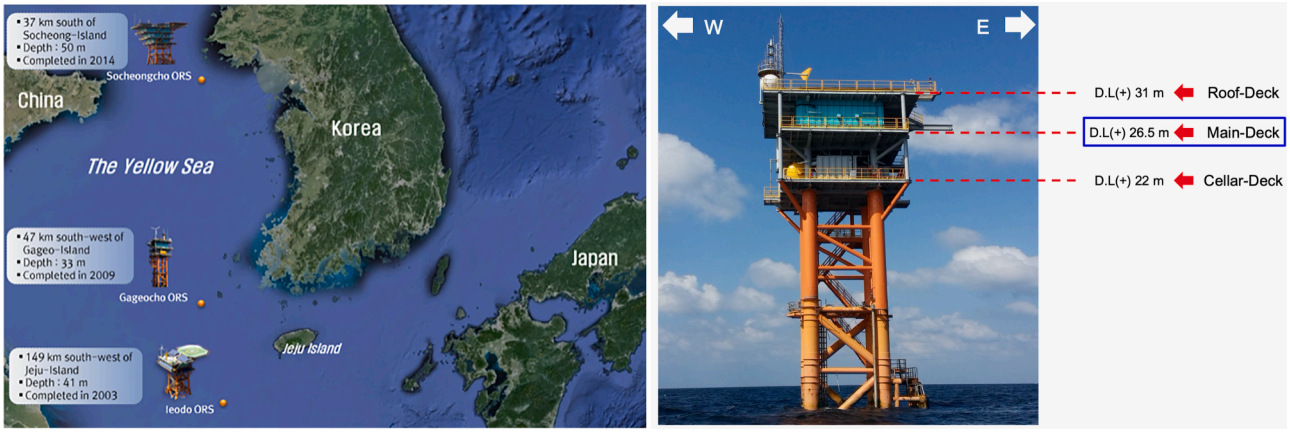

Fig. 1. (left) Geographical map of the Yellow Sea and the three Korean Ocean Research Stations (ORS). Gageocho ORS is located on the east of the southern edge of the Korean peninsula at geographical coordinates (33° 56′ 33″ N, 124° 35′ 35″ E) and mean depth of 33 m. (right) Lateral view of Gageocho ORS. Stereo cameras were installed on the main deck at 26.5 m above the mean sea level, on the east side of the super-structure.

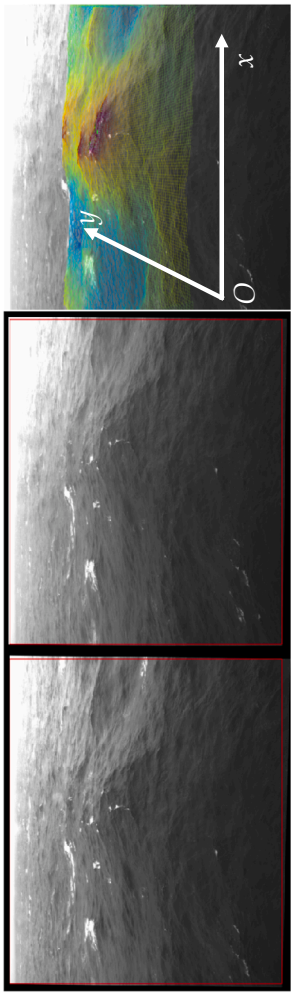

Fig. 2. Example of the stereo wave imaging process. Left stereo image (left), right stereo image (middle), and (right) corresponding wave field $\eta(x, y)$ (shading proportional to the surface elevation, yellow–red colours for wave crests and green–blue colours for wave troughs) collected on 6 October 2018 at 01 UTC. The direction of the horizontal coordinated x- and y-axis is sketched (the axes' origin O is translated only for graphical purposes). The positive y-axis points to the east (dominant waves are coming approximately from the north, moving towards the positive x-axis). As for the size of the observed sea surface region, we refer to the elevation map displayed in Fig. 6.

GORS and the Korean peninsula. We selected one record collected on 5 October (acquisition started at 04 UTC) and seven records collected on 6 October (acquisitions started at 01, 02, 03, 04, 05, 07, and 08 UTC) for the final analysis. These bursts stood out as the highest quality out of twenty sequences acquired, and for them the 3D wave fields $\eta(x, y, t)$ were computed for their total duration.

Wave data were complemented with averages (over 10 min) of wind speed and direction recorded from GORS at 41-m height with a YOUNG Wind Monitor MA (Model 05106) sensor; its nominal accuracy is $\pm$ 0.3 m/s (speed) and $\pm$ 3° (direction). To be compared to model results, measured wind speeds at the non-standard height were corrected to infer the 10-m reference height speed U_{10} assuming a logarithmic marine boundary layer and a constant drag coefficient.

2.4. Atmosphere and spectral-wave numerical simulations

Wind forcing of high quality is crucial for the performance of numerical wave modelling, and, on the subject, the specification of wind fields for cyclonic conditions is not a straightforward task (Cardone and Cox, 2009). High spatial (horizontal and vertical) and temporal resolutions are often required to follow closely the strong gradients that are characteristic of tropical cyclone circulations and reduce the aliasing effect of wind interpolation on wave models. To cope with these general requirements, to simulate the wind and wave conditions during Kong-rey, we have adopted numerical results from the Integrated Forecasting System (IFS) of the European Centre for Medium-Range Weather Forecasts (ECMWF). IFS-ECMWF is a three-component (atmosphere–ocean-wave) coupled model system that produces high-resolution deterministic and ensemble forecasts with 10-day and 15-day lead-time, respectively. The high-resolution deterministic forecasts (cycle CY45R1) produce hourly wind and wave fields at a horizontal resolution of 0.1° (about 9 km × 11 km in the study area) and 0.125° (about 12 km × 14 km), respectively.

The ocean wave directional spectra $S(f, \theta)$ are simulated by the ECMWF version (called ECWAM; ECMWF, 2018) of the third-generation phase-averaged WAM wave model (Komen et al., 1994), forced by 10-m height neutral wind speeds and two-way coupled to the atmosphere and ocean models. ECWAM solves the radiative transfer equation to predict the generation, evolution, and dissipation of ocean surface waves. The wave model runs on a spectral domain with 36 frequencies ($f_1 = 0.0345$ Hz with 1.1 geometric progression) and 36 evenly (10°) spaced directions from 5° to 355°N. The wind input and dissipation source terms are parametrized following the work of Janssen (1991) accounting also for gustiness and air-density effects. Nonlinear energy transfer among wave components is approximated using the discrete interaction approximation (DIA; Hasselmann et al., 1985). Significant wave height from satellite altimeters and the full directional wave spectrum from satellite SARs are assimilated to correct modelled wave fields and produce more realistic analyses and forecasts.

In this study, the high-resolution operational forecasts of wind and waves have been obtained by the ECMWF archive on a regular grid covering the 22°-41°N and 118°-135°E region, with 0.1° resolution for the zonal and meridional components of U_{10}, and 0.25° resolution for the directional wave spectra $S(f, \theta)$. To closely follow Kong-Rey's evolution, we preferred to adopt the 1-hour resolution of the short-term forecast (from + 1 h to + 12 h) rather than the coarse 6-hour analysis fields. Wave moments m_{abc} and related parameters were computed from the model directional spectrum. The model estimation of the total significant wave height $H_s = 4\sqrt{m_{000}}$ from the zeroth-order moment m_{000} of $S(f, \theta)$ is consistent with the value obtained from stereo data and it will be indicated with the same symbol as later used for observations.

IFS-ECWMF represents the state-of-the-art numerical weather prediction. It is currently used to study the genesis and evolution of tropical cyclones (tropical depressions, tropical storms, hurricanes and typhoons; see https://www.ecmwf.int/en/forecasts/charts/latest-tropical-cyclones-forecast; latest visit on 20 June 2021). IFS-ECMWF was proved

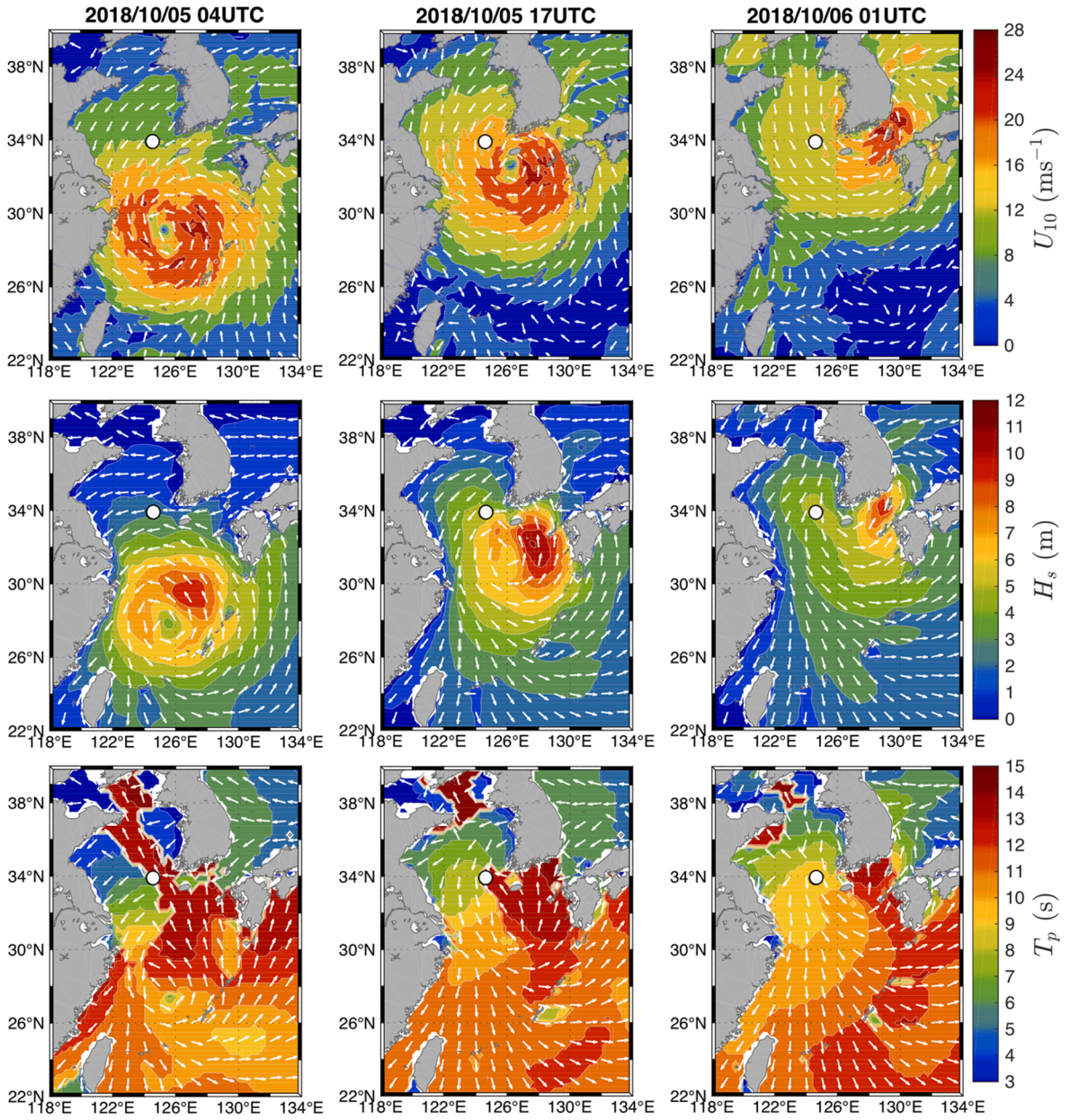

Fig. 3. Wind and wave conditions in the East China Sea and the Yellow Sea during the tropical storm Kong-rey on 5 October (at 04 and 17 UTC) and 6 October (at 01 UTC) 2018. (top) Near-surface (10-m height) wind speed U_{10} (coloured shading; scale on colour bar in units of m/s) and direction (arrows, decimated for graphical purposes). GORS is shown with a white dot, south-west of the Korean peninsula. (middle) Significant wave height H_s (coloured shading; scale on colour bar in units of m) and mean wave direction (arrows, decimated for graphical purposes). (bottom) Directional spectrum peak period T_p (coloured shading; scale on colour bar in units of s) and peak wave direction (arrows, decimated for graphical purposes).

to be particularly skilful in forecasting hurricane tracks but less performant in predicting hurricane intensity, i.e., the minimum surface pressure in the centre of the cyclone or the maximum sustained wind speed at 10-m height within the cyclone (Rodwell et al., 2015; Yamaguchi et al., 2015). Assessing the performance of IFS-ECMWF with all the tropical cyclones in 2017, Magnusson et al. (2019) showed that it tends to produce too intense pressure minima and too weak maximum wind speeds. Therefore, significant efforts are being undertaken to tailor the global model configuration to such severe events as hurricanes and typhoons. As for waves generated in these conditions, a limiter for the maximum spectral steepness has been implemented in ECWAM, leading to a more consistent representation of the drag coefficient and surface roughness when U_{10} exceeds 25 m/s (see, e.g., Powell et al., 2003).

It has been stated in previous studies (e.g., Young, 2017) that, during tropical cyclones, wind input and nonlinear interactions control the shape of the 2D frequency/direction spectrum, which is one of the key issues in spectral wave modelling (Cavaleri et al., 2020, 2007; Liu et al., 2017; Stopa et al., 2016). There are many sources of error, but the nonlinear wave-wave interaction modelling using the DIA is known to be responsible for broadening the spectrum in frequency and direction compared to the exact interaction (Rogers and Van Vledder, 2013). DIA can also give rise to systematic errors of bulk parameters such as H_s under hurricane conditions (Tolman, 2013). Although our understanding of the central role that nonlinear interactions play in determining the shape of the ocean wave spectrum has advanced significantly, since their effects may influence the wave spectrum variables that are used in the formulations of extremes, in this study, we have used the set of observed spatio-temporal wave fields for a comparison with the wave model outputs.

To complete this section, it is necessary to point out the difference at

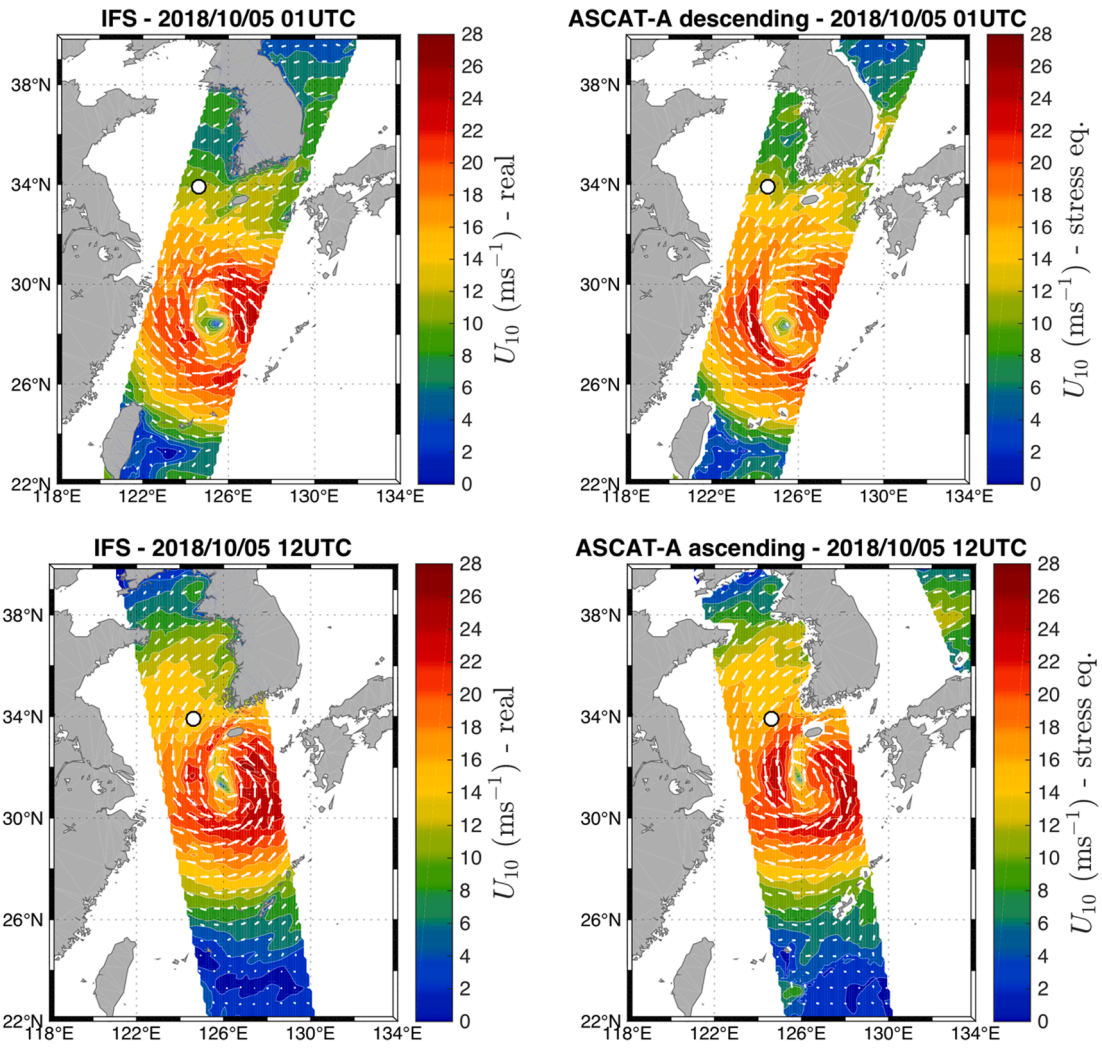

Fig. 4. Surface wind speed U_{10} (coloured shading; scale on colour bar in units of m/s) and direction (arrows, decimated for graphical purposes) at 10-m height on 5 October 2018 01 UTC (top) and 5 October 2018 12 UTC (bottom). (left) Model IFS-ECMWF real wind and (right) satellite stress-equivalent wind (ASCAT-A descending at 01:06 UTC, top-right, and ASCAT-A ascending at 12:40 UTC, bottom-right, 0.125° resolution). The position of GORS is shown with a white dot, south-west of the Korean peninsula.

the position of GORS between the bottom depth used by the wave model (91 m) and the actual depth (33 m). Since the ridge on which the station is based is relatively small (few peak wavelengths in stormy conditions) and surrounded by an almost flat bottom at 90 m, we expect a slight modification of the propagating wave energies because of their interaction with the local rise. However, for the computation of the spectral wave steepness, some differences may exist, as we have specified in section 2.2. This notwithstanding, in the remainder of this paper, we have adopted (for model and observed data) a deep-water formulation for μ based on the reasoning that during Kong-rey (*i*) the use of an intermediate-water formulation will provide values within 10% of those for deep waters, (*ii*) in intermediate waters, about the same difference is expected by imposing either 91 m or 33 m, and (*iii*) the deep-water formulation includes the spectral width information, which is relevant when comparing model and observed wave spectra.

3. Results and discussion

In this section, we shall focus on analysing the wave fields in the Northwestern Pacific on 5 and 6 October 2018 when the tropical storm Kong-rey translated north towards the Korean peninsula, and measurements from GORS are available, permitting a local assessment and a direct comparison with model results. The objective is threefold. On the one hand, models are used to give an overview of the cyclone and the structure of the sea wave response (intensity and pattern), and, on the other hand, the comparison with observations allows for verifying the wave model performance in terms of the directional spectrum parameters (such as significant wave height, steepness, spectral width, and directional spread) that enter the formulations for spatio-temporal wave extremes. Finally, extremes from observations and model results are compared, and the latter is used to describe the maximum wave statistics during the storm.

3.1. Wind and wave fields

The model fields of U_{10} and H_s in the East China Sea and the Yellow Sea are shown in Fig. 3 for the dates of 5 October 2018 at 04 UTC (left) and 6 October at 01 UTC (right), when concurring stereo observations are available, and of 5 October 17 UTC (middle), when peak conditions for modelled H_s were reached south of the Korean peninsula, just west of Kyushu (Japan). As winds rotated counterclockwise around the cyclone eye, the highest wind speeds (about 28 m/s) occurred in the north-east quadrant, where they generated the highest waves (H_s up to 12 m on 5 October at 17 UTC). Unlike typical, open-sea conditions for cyclones (Young, 2017), the wave field's spatial extent was constrained by the coast and not larger than the wind field, and contours of wave fields

Table 1
Observed wave parameters at GORS on 5 and 6 October 2018. Significant wave height H_s; skewness coefficient λ_3; mean spectral steepness μ; normalized minimum of the auto-covariance function ψ^*; determinant det(Λ) of the covariance matrix of the sea surface elevation gradient; average value and standard deviation *std* of the maximum wave height $\overline{H}_{\max,o}$ and maximum crest height $\overline{C}_{\max,o}$ over a spatio-temporal cuboid of square area $XY = 60$ m $\times$ 60 m and duration $D = 180$ s.

Record	Date (2018)	H_s (m)	λ_3 (-)	μ (-)	ψ^*(-)	det(Λ)	$\overline{H}_{\max,o} \pm std$ (m)	$\overline{C}_{\max,o} \pm std$ (m)
1	5 Oct. 04 UTC	2.74	0.10	0.058	−0.50	4.54e-05	5.38 ± 0.33	3.38 ± 0.30
2	6 Oct. 01 UTC	4.70	0.15	0.060	−0.65	1.09e-04	8.26 ± 0.90	5.13 ± 0.41
3	6 Oct. 02 UTC	4.27	0.12	0.058	−0.65	1.05e-04	7.50 ± 1.07	4.79 ± 0.43
4	6 Oct. 03 UTC	3.98	0.14	0.061	−0.63	1.04e-04	7.19 ± 0.54	4.68 ± 0.42
5	6 Oct. 04 UTC	3.88	0.14	0.056	−0.64	6.26e-05	6.71 ± 0.75	4.41 ± 0.52
6	6 Oct. 05 UTC	3.70	0.12	0.058	−0.65	4.26e-05	6.58 ± 0.60	4.16 ± 0.33
7	6 Oct. 07 UTC	3.47	0.14	0.055	−0.66	2.17e-05	6.11 ± 0.78	3.96 ± 0.67
8	6 Oct. 08 UTC	3.40	0.13	0.054	−0.64	2.04e-05	6.30 ± 0.42	4.06 ± 0.37

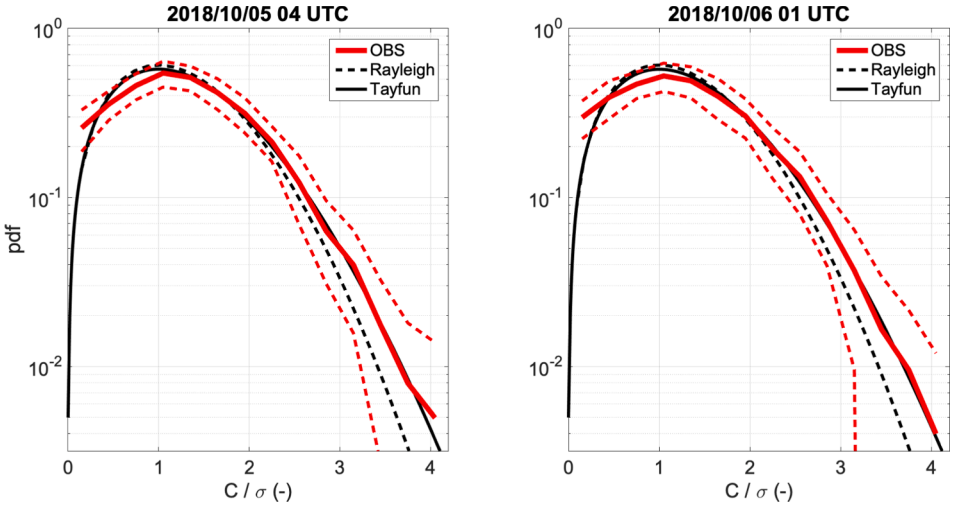

Fig. 5. Probability density function (pdf) of normalized crest heights C/σ from observations (OBS) on 5 October 2018 at 04 UTC (left) and on 6 October 2018 at 01 UTC (right). The red line shows the average density out of fifty time series evenly chosen over an area 60x60 m^2 taken at the centre observed *xy*-space. Dashed red lines show the uncertainty of the estimates. Empirical data are compared with the linear Rayleigh (dashed black line) and the second-order nonlinear Tayfun (solid black line) models.

were left behind the propagating storm centre. During its course, the storm crossed the East China Sea from south to north (we have estimated that the cyclone's forward speed averaged around 8 m/s), and, after landfall, it left the Yellow Sea to the west. Wind conditions changed on 5 and 6 October, becoming more northerly as the cyclone moved north-eastward. Maximum values of H_s eventually channelled through the Korea Strait, where H_s up to 9 m was modelled.

The common wind-wave misalignment under cyclonic conditions may be depicted in the bottom panels of Fig. 3, where the wave peak direction and period are shown. In the Yellow Sea, between Korea and China, on 5 October, the central part of the basin was dominated by long swell waves (from south-east, radiating from a region on the right of the cyclone), while near the coasts (east and west sides) the shorter wind-sea from north-east was responsible for the more energetic sea states. These conditions changed as the cyclone moved the north-east later on 5 October, when the wind-sea became dominant.

For a qualitative evaluation, Fig. 4 shows a comparison between the model 10-m height winds (left) and the satellite-borne Advanced Scatterometer (ASCAT-A) products (right). Despite the different type of wind (real, for the model, and stress-equivalent, for the observation) and that the ASCAT datasets are assimilated in the atmospheric model analysis, we observe that the scatterometer winds are propagated further into the forecast, which therefore gives a consistent position and pattern of the cyclone winds. However, some local differences may remain that may explain the difference we observed at the GORS position (Fig. 7).

3.2. Wave observations at GORS

3.2.1. Sea-state statistical and spectral parameters

The stereo wave measurements of the spatio-temporal surface elevation field $\eta(x,y,t)$ have been used with the dual aim of characterizing the sea states in the southern Yellow Sea (GORS location) and of assessing wave model results. The standard deviation σ of the wave field has been estimated from the second-order moment of the empirical probability density function of $\eta(x,y,t)$ as follows:

$$\sigma^2 = < [\eta(x,y,t) - < \eta(x,y,t) >]^2 > \quad (18)$$

where the angle brackets $< >$ denote the ensemble average, and the observed significant wave height has been approximated, for each record, as $H_s = 4\sigma$ (Table 1). From observations, H_s was maximum (4.70 m) on 6 October at 01 UTC, then decreased following the north-east course of Kong-rey. However, higher values were likely reached late on 5 October (see Fig. 7) when stereo observations were not available. We anticipate that, from the analysis of model spectra (section 3.4), the elevation variance at GORS during all stereo acquisitions was dominated by the locally generated wind waves whose amplitudes and phases were modulated at short scales by a swell.

The relevance of deviations from Gaussianity due to the second-order nonlinear bound harmonic waves (which do not satisfy the linear dispersion relation; see Fig. A1) is manifested in a non-zero and positive skewness coefficient λ_3 that was determined from the measured wave field as follows:

$$\lambda_3 = < \left[\frac{\eta(x,y,t) - < \eta(x,y,t) >}{\sigma} \right]^3 > \quad (19)$$

Values of λ_3, reported in Table 1, show that the departure of the process from Gaussianity was minimum ($\lambda_3 = 0.10$) on 5 October at 04 UTC; afterwards, λ_3 peaked at 0.15 on 6 October at 01 UTC, and values between 0.12 and 0.14 characterized the following sea states.

In accordance with the numerical model, the wave field *steepness* μ and *bandwidth* ψ^* have been computed from the observed energy spectra S in terms of intrinsic frequencies f (see Appendix A).

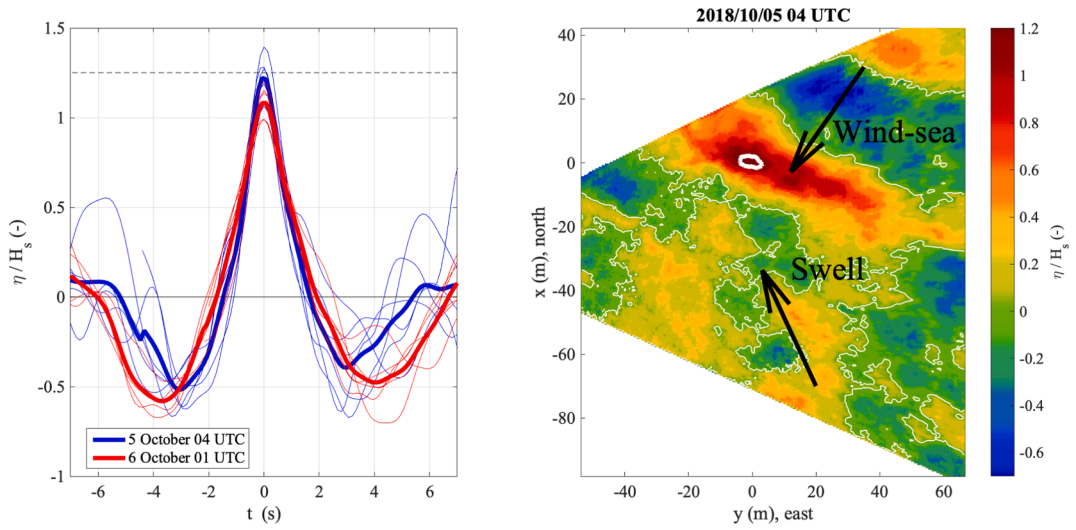

Fig. 6. Shape of the observed maximum waves in the Yellow Sea at the GORS location. (left) Individual (thin lines) and average (thick line) temporal profiles (normalized with H_s) of the waves with the highest sea surface elevation (crests heights) on 5 October at 04 UTC (blue) and on 6 October at 01 UTC (red). Profiles are shifted by imposing as time $t = 0$ the instant of the maximum surface elevation $\max\{\eta(t)\}$. The dashed black line shows the rogue wave threshold $\eta = 1.25H_s$ for crest heights. (right) Normalized 2D wave field $\eta(x, y)/H_s$ from the record observed on 5 October 2018 at 04 UTC at time of the global maximum $\max\{\eta(x, y, t)\} = 1.39H_s$, set at coordinates $(x, y) = (0, 0)$ for graphical purposes. The thick white contour around (0, 0) bounds the region where $\eta > 1.25H_s$, and the thin white contour shows the still-water elevation level $\eta = 0$. The black arrows indicate the peak direction of the wind-sea (from the north-east) and swell (from the south-east) from spectral wave model results.

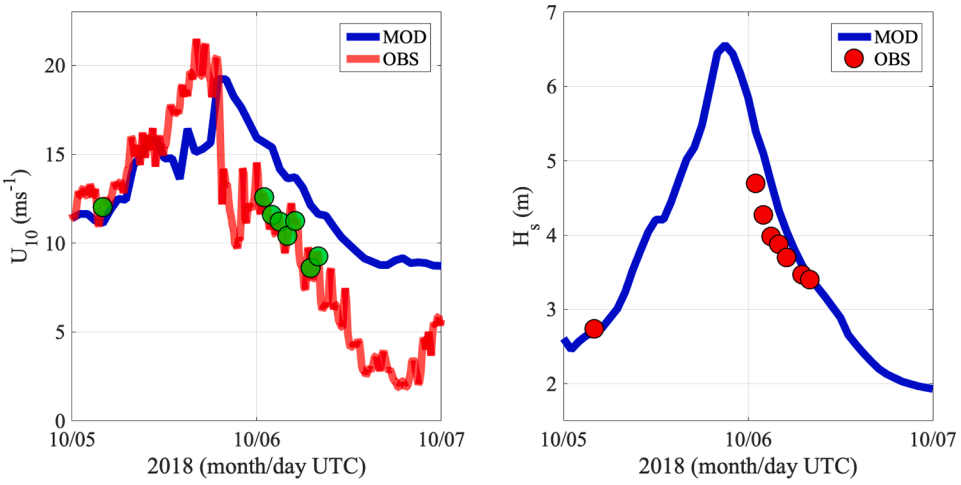

Fig. 7. Wind and wave evolution at the Gageocho Ocean Research Station (GORS) during the tropical storm Kong-rey (5 and 6 October 2018). (left) Evolution of the 10-m height wind speed U_{10} from IFS-ECMWF model (MOD, blue line) and observational data (OBS, red line). The green dots depict the wave observations with WASS available on 5 October at 04 UTC and 6 October at 01, 02, 03, 04, 05, 07, and 08 UTC. (right) Evolution of the significant wave height H_s from ECWAM model (MOD, blue line) and WASS observational data (OBS, red markers).

Concerning the directional properties of the wave field $\eta(x, y, t)$, as stated in section 2.2, they may be expressed in terms of the determinant $\det(\Lambda)$ of the covariance matrix of the sea surface elevation gradient. For the model, values of $\det(\Lambda)$ have been estimated from the moments m_{abc} of the directional wave spectrum, while the covariance matrix and its determinant have been calculated in the 3D physical *xyt*-space using the observed elevation data (Table 1). For the latter, the local and instantaneous 3D gradient vector $\nabla\eta = (\eta_x, \eta_y, \eta_t)$ has been computed by finite, central difference approximation over the discrete spatial and temporal axes.

We conclude this section by remarking that the steepness μ (from observations and later in this study from model results) has been determined using the moments of the wave spectrum of all waves, which represent combined swell and wind-sea wave fields. Therefore, a point must be raised on which form should take the characteristic total steepness since a unified formulation of spectral parameters that accounts for multimodal sea states is far from being trivial (see, e.g. Støle-Hentschel et al., 2020). Said this, to allow the comparison between model results and observations, we have not employed frequency/direction partitions, and we have computed a global steepness from the spectrum $S(f)$, as given in Eq. (11).

3.2.2. *Spatio-temporal maximum waves*

We are here interested in isolating the highest waves observed in the stereo records and measuring their heights C_{max} and H_{max}. Firstly, Fig. 5 shows the empirical probability density function of individual crest heights C in time series for two different stereo records. For reference, the linear Rayleigh and nonlinear Tayfun (1980) models are compared. The latter, which accounts for the contribution of the second-order bound waves in the sea elevation, describes well the observed statistics of the highest crests.

As pointed out in previous studies (Benetazzo et al., 2021), for extreme wave sampling, a set of independent realizations must be assembled to simulate the stochastic process and provide an assessment of the theoretical formulations. For wave observations at GORS during the tropical storm Kong-rey, we have then split each of the eight records $\eta(x, y, t)$ in adjacent and non-overlapping chunks by choosing 3D domains $\Gamma_s := [0, X] \times [0, Y] \times [0, D]$ of equal spatial sides $X = 60$ m and $Y = 60$ m, and duration $D = 180$ s rolling over the temporal axis. Over each Γ_s, the global maximum crest height is defined as follows:

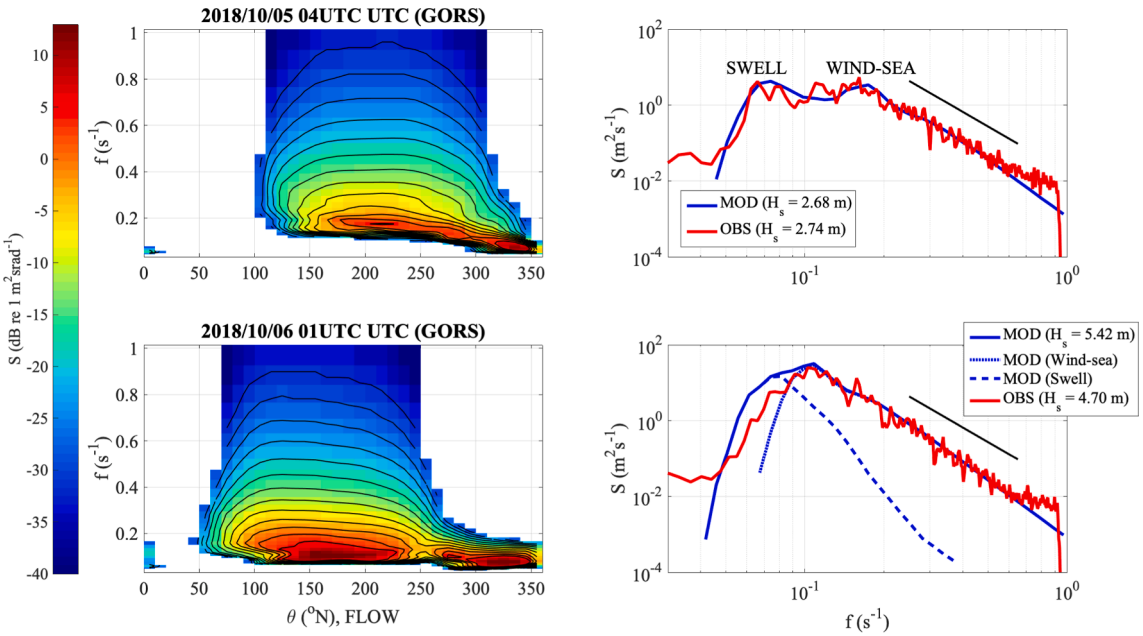

Fig. 8. Frequency/direction $S(f, \theta)$ and omnidirectional (azimuth-integrated) frequency $S(f)$ wave spectra at GORS on 5 October at 04 UTC (top) and on 6 October at 01 UTC (bottom). In the right panels, model (MOD) and observed (OBS) frequency spectra are depicted, and in the bottom-right panel the dotted and dashed blue lines show the wind-sea and swell contribution to the total wave energy, respectively. The value of H_s is given in the insets. In the right panels, the solid black line represents the reference slope proportional to f^{-4}.

$$C_{\max,s} = \max\{\eta(x,y,t)|(x,y,t) \in \Gamma_s\} \tag{20}$$

while the maximum wave height $H_{\max,s}$ for $(x, y, t) \in \Gamma_s$ was measured via zero-crossing analysis of each time series $\eta(t)$ of duration D defined within the xy-space $\in [0, X] \times [0, Y]$. The two sets of random variables $\{C_{\max,s}\}$ and $\{H_{\max,s}\}$ have an empirical distribution function, of which we have computed the sample averages (Table 1) given by

$$\overline{C}_{\max,o} =< C_{\max,s} >$$

$$\overline{H}_{\max,o} =< H_{\max,s} > \tag{21}$$

to be compared with the theoretical expectations $\overline{C}_{\max}$ and $\overline{H}_{\max}$, respectively (see section 3.6.1).

For the time being, we report that $\overline{C}_{\max,o}$ ranged between $1.09H_s$ and $1.24H_s$, and $\overline{H}_{\max,o}$ between $1.73H_s$ and $1.97H_s$. The highest level of wave extremity was reached, on average, on 5 October at 04 UTC, when the observed H_s was minimum (2.74 m); within the same record, the individual highest values were identified and had $\max\{H_{\max,s}\} = 2.09H_s$ and $\max\{C_{\max,s}\} = 1.39H_s$. On the contrary, and as it was largely expected, the set of highest waves ($\overline{C}_{\max,o} = 5.13$ m $= 1.09H_s$, and $\overline{H}_{\max,o} = 8.26$ m $= 1.76H_s$) was measured when the observed H_s peaked on 6 October at 01 UTC.

A comparison between the shape of the highest waves at different times is shown in Fig. 6 (left panel), which depicts the temporal profiles $\eta(t)$ normalized with H_s of the individual waves with the highest sea surface elevations on 5 October at 04 UTC (blue lines) and on 6 October at 01 UTC (red lines). The shapes exhibit clear nonlinear behaviour with a steep wave crest and flat wave troughs. We note that on 5 October, the measured waves were apparently more extreme than those on 6 October. Since the characteristic steepness was very similar (about 0.06), we may anticipate that most of the differences stem from the domain size for extremes. Indeed, following the growth of H_s from 5 to 6 October, waves become progressively longer (as it is depicted in Fig. 6), therefore the sample size N_{3D} decreased (indeed, X, Y and D were kept constant), and, consequently, the value of the sampled extremes was (on average) smaller. We note that both average profiles (thick lines) display asymmetry of the troughs around the central crest, likely due to a lack of perfect phase coherence at the focusing of wave groups that is expected for finite and large amplitudes (Fedele et al., 2020).

Finally, the right panel of Fig. 6 depicts the individual wave field $\eta(x, y)/H_s$ from the record observed on 5 October 2018 at 04 UTC at the instant when $\eta = \max\{\eta(x, y, t)\} = 1.39H_s$, which may qualify as belonging to a rogue wave. We observe that the wave with the maximum elevation is relatively short-crested and propagates with the wind sea (from the north-east). A contribution due to the crossing swell (from the south-east) is concurrent and modulates the local surface elevation's rise.

3.3. Models' performance at GORS

Fig. 7 shows the time series comparison at the GORS position of model results (MOD) and observations (OBS) of U_{10} and H_s. Wind speed data indicate that the wind growth was followed by a rapid decay because of the north-east trajectory of the storm winds passing over the Korean peninsula. The atmospheric model progressively underestimated (up to about 5 m/s) the observations during the growing phase of the wind intensities, while the opposite (i.e., model overestimation) happened during the decaying stage when $U_{10} < 20$ m/s. This implies that, while there was a good match early on 5 October (absolute difference smaller than 1 m/s), later on 6 October, the model minus observation bias was positive and about + 3 m/s. As for the significant wave height (right panel), the wave model responded the same way (i.e., the model overestimated observations on 6 October), and after the model peak (equal to 6.56 m, on 5 October at 21 UTC), the H_s bias is on average about + 0.5 m (+11%) regarding observations. Since, as we pointed out before, the significant wave height is the leading scale factor for extremes, this error metrics will be considered when evaluating the model performance with regard to the maximum waves.

3.4. Wave spectra

Close to the southern edge of the Yellow Sea, the peculiarity of the coupled wind-sea/swell system resulting at the position of GORS is shown in Fig. 8, which depicts, at two different instants, the cyclone-

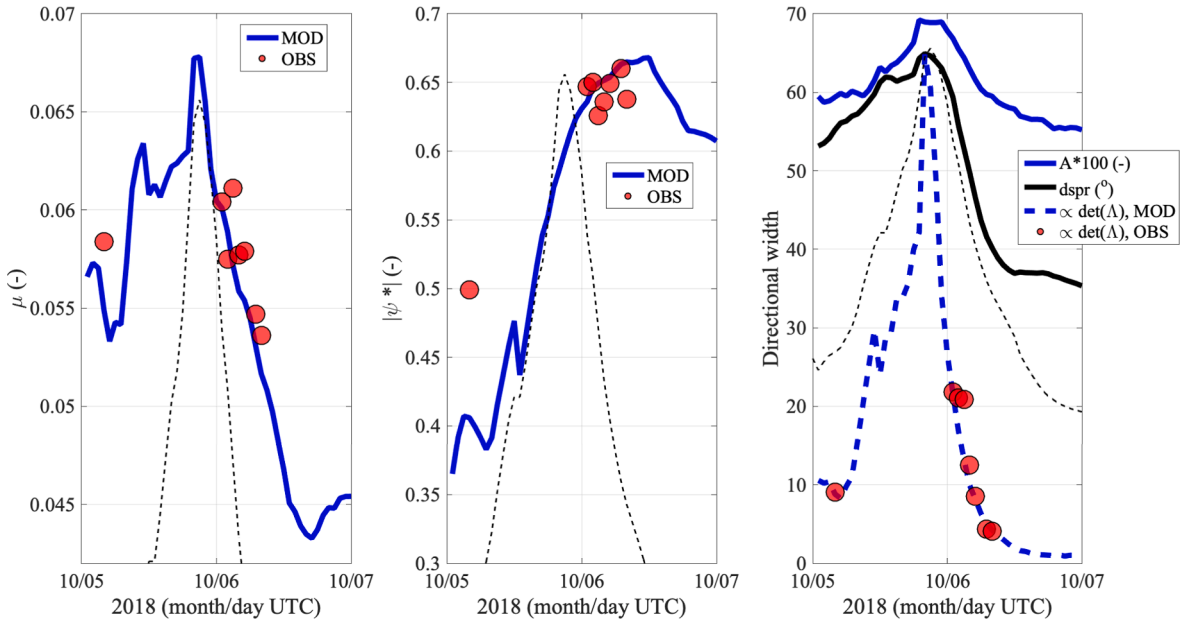

Fig. 9. Sea state parameters at GORS on 5 and 6 October 2018 from the model (blue line, MOD) and observations (red markers, OBS). (Left) Mean wave steepness μ; (middle) absolute value of the normalized minimum ψ^* of the autocovariance function of the sea surface elevation; (right) mean directional spread *dspr*, 3D width parameter A, and determinant of the covariance matrix Λ of the 3D surface elevation gradient. Values of A and det(Λ) are scaled by a constant value for graphical purposes. In all panels, the dashed black line shows the time history of the model H_s shown in Fig. 7 (scaled in each panel for graphical purposes).

induced directional $S(f, \theta)$ and azimuth-integrated omnidirectional frequency $S(f)$ spectra from model (MOD) and observations (OBS). Since during Kong-rey, GORS (depicted with a white dot in Fig. 3) was positioned in the farther left-front quadrant while the cyclone's eye moved north-eastward, at that position we expect waves from swell and winds to be misaligned, with a local condition turning from a cross to opposing swell (Holthuijsen et al., 2012; Liu et al., 2017)

At the time of the WASS observation on 5 October at 04 UTC (top panels of Fig. 8), the 2D directional spectrum was skewed and bimodal in frequency and direction (resembling the "Type I" spectral shape of Hu and Chen, 2011, during Hurricane Rita) with two clearly separated, crossing wave systems. At first, a narrow peak induced by the swell propagated towards 335°N (flow direction) with a period of 13.5 s (0.074 Hz, relative depth $kd = 2.1$), radiating out from the region to the right of the moving cyclone centre where the winds were very intense. Then, we depict a broader system for the local wind-sea, with a peak period of 5.7 s (0.1745 Hz) and propagating, with slight directional deviation to winds, towards 215°N (i.e., crossing the swell at 120°). The two systems are distinct also in the omni-directional 1D frequency spectrum (top-right panel), both from the model (blue line) and from the observations (red line) that produce very similar energy contents. We note that a bimodal shape of $S(f)$ is typical for areas at a large distance from the centre of a cyclone.

Later, on 6 October at 01 UTC (bottom panels of Fig. 8), when GORS was closer to the storm centre, the energy spread in almost all directions. The local wind-sea turned north-westerly (165°N at the peak) and displayed more energetic and longer waves (9.2 s period at the peak, i.e. frequency of 0.1083 Hz). The swell, generated at a southern location at a somewhat earlier time, changed its dominant direction (325°N) slightly, therefore producing an opposing swell condition (the separation angle is 160°). Because of the small separation between swell and wind-sea carrier frequencies, the 1D frequency spectrum $S(f)$ is unimodal (bottom-right panel) with a smooth transition between swell and wind-sea, which accounts for about 75% of the total energy. The unimodality is a common feature of all frequency spectra at GORS (not shown here) from this date onwards. The comparison with observation (red line) shows that the model overestimated energy of the longer wave components (mostly from swell) at frequencies smaller than the peak (0.1083 Hz), while the high-frequency face of the omni-directional spectra decays approximately with the reference slope f^{-4} (Zakharov and Filonenko, 1967). The sea states underpinning these two spectral conditions impact on the sea state parameters and on wave extremes, as we shall describe in the following sections.

3.5. Parameters of the extreme value distributions

In this section, we shall concentrate on the sea state parameters that enter the formulations for extremes. A description of their evolution at GORS and a local comparison between observed (Table 1) and model data are provided. We begin by analysing the parameters that are computed in terms of integral quantities from the omni-directional frequency spectrum $S(f)$.

The model-to-observations comparison of the *steepness* μ is shown in the left panel of Fig. 9. In particular, after having peaked the observed μ at 0.061 on 6 October at 03 UTC, the wave steepness steadily decreased on 6 October (overall change around 10%). Model values (blue line) experienced a progressive growth on 5 October following the cyclone's northward development (indeed, for cyclones, the steepest sea states are generally located in the rear of the eye; Holthuijsen et al., 2012), and it peaked at 0.068 when the local significant wave height was maximum (dashed black line in all panels). Since then, the value of μ decayed rapidly as the cyclone passed over the Korean peninsula on 6 October. The comparison against observations shows that the model reproduced well the wave steepness at the different stage of the cyclone development and wave spectrum evolution: the model minus observation relative bias is negative and equal to −3%, i.e., the model slightly underestimated the observations.

As for the *bandwidth* parameter $|\psi^*|$ (middle panel of Fig. 9), the observed value was minimum (0.50) on 5 October at 04 UTC (indeed the frequency spectrum in Fig. 8 shows a well distinct bimodal shape), then increased on 6 October (0.65, on average), accompanying a narrowing of the frequency spectrum. The model evolution of $|\psi^*|$ shows that it started growing with H_s but exhibited a different behaviour afterwards, by peaking a few hours later than H_s and remaining above 0.6 after the storm passed east of the station. On 5 October, values were between 0.4 and 0.5, typical of a broad frequency spectrum with wind waves

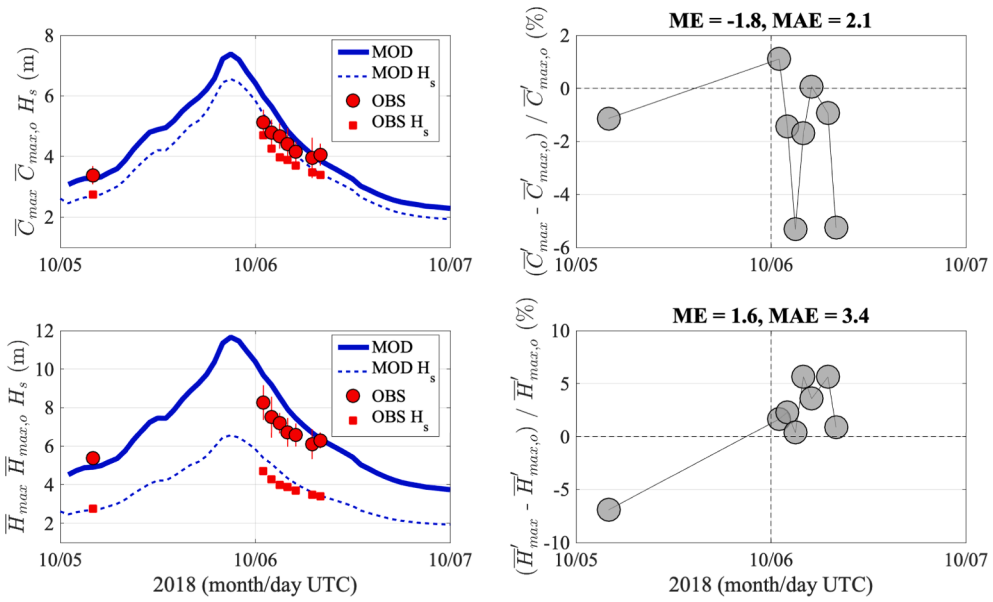

Fig. 10. Maximum waves at GORS during the tropical storm Kong-rey (5 and 6 October 2018). (left) Observed (OBS, red circles) and modelled (MOD, solid blue line) maximum crest (top-left) and wave (bottom-left) heights. The spatio-temporal domain Γ has size $V = 60$ m $\times$ 60 m $\times$ 180 s. The vertical red bars show the standard deviation of the observations. The dashed blue line depicts the model H_s and the red squares the observed values. (right) Percentage difference between modelled and observed extremes. The variables normalized with the significant wave height are indicated with a prime mark. Error metrics: mean relative error (ME) and mean relative absolute error (MAE).

superimposed to a swell (Boccotti, 2000). Then, later on 6 October, when the wind waves dominated, and the frequency spectrum narrowed (indeed $\psi^* = -1$ in the limit of an infinitely narrow spectrum), the bandwidth $|\psi^*|$ was indeed greater and in excess of 0.6 (in good agreement with observations). We note that the negative model-minus-observation difference of $|\psi^*|$ (about -20%) on 5 October cannot be fully explained by the model mismatch in representing the evolution of the cyclone winds at GORS. On the other hand, a single value cannot provide indications of whether the reason was the DIA affecting, i.e., broadening, the frequency spectrum. However, for extreme estimates, everything else being equal (i.e., H_s and *sample size*), this mismatch would produce marginally smaller values of the modelled maximum wave heights.

The directional properties of the wave field are less easily assessed using the stereo data. Indeed, these data spans a surface area that usually is not wide enough to allow for a direct computation of the directional spectrum for the peak wave components. Therefore, in the Fourier 3D space (k_x, k_y, f), only short-to-medium wavelength components are adequately represented (Peureux et al., 2018), unless statistical models are used to retrieve the unresolved spatial scale (Benetazzo et al., 2018b; Leckler et al., 2015). We have therefore relied on the physical 3D space (x, y, t) and adopted a different strategy to assess the directional properties, which is also consistent with the input to the formulations for wave extremes. Indeed, as we pointed out in section 2.2, the three coefficients α_{xt}, α_{yt}, α_{xy} of the determinant of the covariance matrix Λ of the surface elevation 3D gradient vector are a measure of the angular spreading due to the contribution of elementary waves propagating from different directions. The value of $\det(\Lambda)$ can therefore be used for comparison.

Results are shown in the right panel of Fig. 9. The mean directional spread *dspr* is estimated as (Kuik et al., 1988)

$$dspr = \sqrt{2\left(1 - \frac{\sqrt{s^2 + c^2}}{m_{000}}\right)} \tag{22}$$

where

$$s = \iint \cos(\theta) S(\omega, \theta) \mathrm{d}\omega \mathrm{d}\theta \tag{23}$$

$$c = \iint \sin(\theta) S(\omega, \theta) \mathrm{d}\omega \mathrm{d}\theta \tag{24}$$

We note that model values of *dspr* (solid black line), which peaked at 65°, and width parameter A (solid blue line, scaled of a factor of 100 for graphical purposes) show similar behaviour (the linear correlation coefficient is 0.9) and follow closely the growing and decaying phases of the cyclone at GORS (there is a good match with the H_s history; dashed black line). However, since the value of A depends on the axis orientation of the spatio-temporal 3D cuboid (Baxevani and Rychlik, 2004), its comparison between model and observations is not straightforward, given the different orientation existing between the model geographical axes and the observation spatial xy-grid. On the contrary, the value of the determinant $\det(\Lambda)$ of the covariance matrix is not affected by a rigid rotation of the axes (Benetazzo et al., 2017b). This property has been therefore used to compare (right panel of Fig. 9) its values derived from the model directional spectrum (dashed blue line) and from spatio-temporal observed wave fields (red markers). We note a very good agreement for this variable, with a modest model underestimation of about -8%.

To sum up, evaluation of model results at GORS reveals that the frequency/direction spectrum parameters are consistent with observations. During the decaying phase of Kong-rey, however, the wave model underestimated the significant wave height due to a bias in the local wind forcing. With this in mind, the following analysis of wave maxima focuses, on the one hand, on further model performance assessment and, on the other, on the characterization of extremes at the basin scale.

3.6. Maximum waves under the cyclone winds

In this section, we shall focus on the maximum wave statistics during Kong-rey by analysing three different conditions for the characterization of extremes and sets of data. Firstly, a comparison between modelled and observed values of $\overline{H}_{\max}$ and $\overline{C}_{\max}$ is performed using the 3D wave fields measured from GORS on 5 and 6 October 2018; secondly, modelled spectra in the East China Sea and the Yellow Sea are used to estimate the maximum waves that may occur over a fixed-size domain Γ; finally, this examination is made by adopting a domain of variable size, which we impose as dependent on the characteristic spatio-temporal scales of the local and instantaneous sea state (namely, L_x, L_y, and T_z). These analyses allow us to gain insight into different mechanisms controlling the spatio-temporal extreme wave formation, as we describe below.

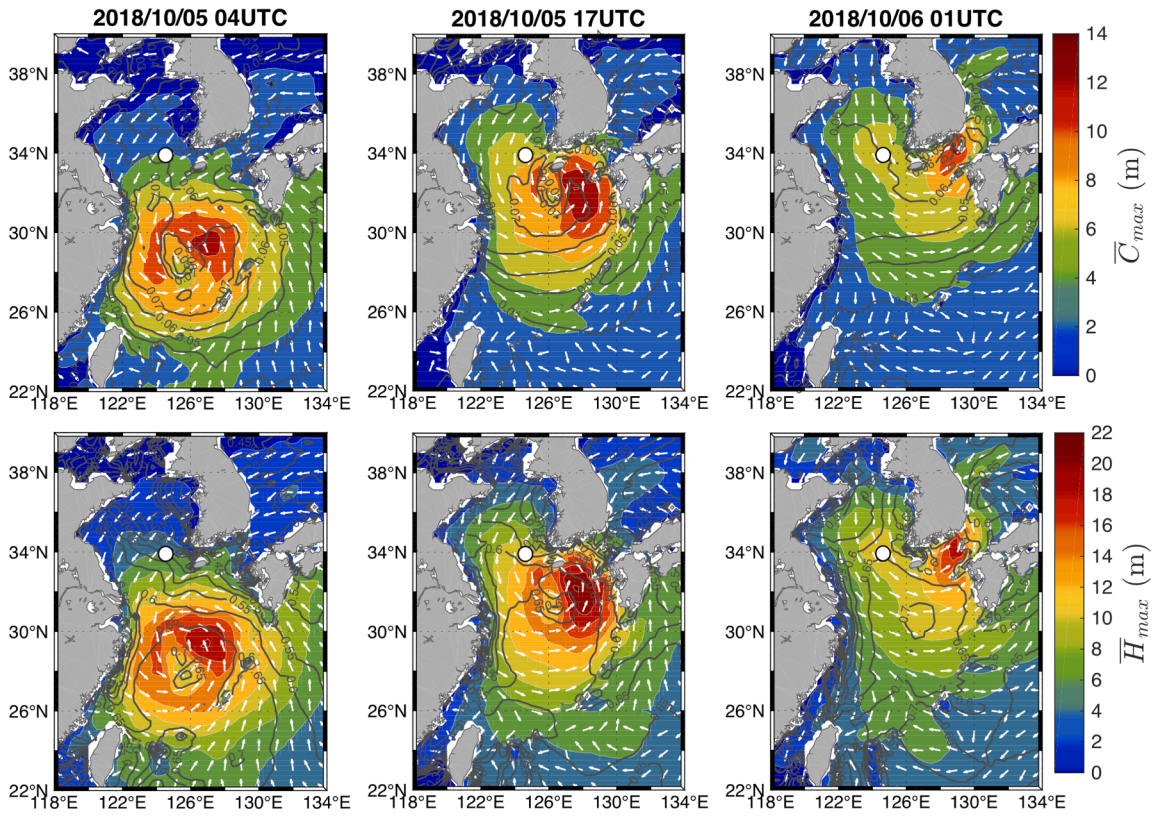

Fig. 11. Maximum waves in the East China and Yellow Seas on 5 October 2018 at 04 UTC (left), on 5 October 2018 at 17 UTC (middle), and on 6 October 2018 at 01 UTC (right). Fixed-size domain Γ for spatio-temporal extreme waves: $X = 100$ m, $Y = 100$ m, $D = 1200$ s. Maximum sea surface elevation (crest height) $\overline{C}_{\max}$ (coloured shading; scale on colour bar in units of m) and maximum sea wave height $\overline{H}_{\max}$ (coloured shading; scale on colour bar in units of m). GORS is shown with a white dot, south-west of the Korean peninsula. Black contours show the wave steepness μ (top) and the bandwidth parameter $|\psi^*|$ (bottom). Arrows (decimated for graphical purposes) depict the U_{10} wind speed vector.

3.6.1. Local analysis

We compare at the GORS position the model maximum wave statistics with observations (Table 1). The spatio-temporal maximum crest height $\overline{C}_{\max}$ and wave height $\overline{H}_{\max}$ are concerned (Fig. 10), which are estimated over 3D regions of sides $X = 60$ m, $Y = 60$ m, and $D = 180$ s. The modelled heights (solid blue line) closely mirror the evolution of H_s (dashed blue line), and they peaked at $\overline{C}_{\max} = 7.4$ m and $\overline{H}_{\max} = 11.7$ m. As pointed out above, most of the differences between observations (red markers) and model data are ascribable to the model overestimation in reproducing the behaviour of the significant wave height. Consequently, on 6 October, we note a positive model minus observations residual, up to about + 0.8 m and + 1.5 m for $\overline{C}_{\max}$ and wave heights $\overline{H}_{\max}$, respectively. As a matter of fact, the errors on the significant wave height jeopardize the capability to fully judge the performance of the numerical model for extremes, as was indicated by Benetazzo et al. (2021).

An effective way to overcome the direct dependence between the sea severity and the extreme wave statistics is to assess the model expectations by normalizing the maximum heights with H_s. In this case (right panels of Fig. 10, where the normalized values are indicated with a prime mark), we observe a fair agreement between model results and observations. The mean relative error (ME) is −1.8% and + 1.6%, and the mean relative absolute error (MAE) is 2.1% and 3.4%, for $\overline{C}_{\max}$ and $\overline{H}_{\max}$, respectively. At times of the stereo measurements, the similarities of the sample averages $< \overline{H}_{\max,o}/H_s > = 1.80$ and $< \overline{H}_{\max}/H_s > = 1.83$, and $< \overline{C}_{\max,o}/H_s > = 1.15$ and $< \overline{C}_{\max}/H_s > = 1.13$ confirm the overall reliability of the model estimations. It is evident the impact on $\overline{H}_{\max}$ of the bandwidth difference on October 5, when the model had the worst skill (underestimation of about 7%). Otherwise, $\overline{H}_{\max}$ errors are clustered around + 3%. As for the maximum crest heights, the model tended to slightly underestimate the observations, reflecting the general behaviour of the wave steepness at GORS during the storm. The third-order nonlinear effects on spatio-temporal extreme crests may be parameterized as a function of the excess kurtosis (Fedele et al., 2017), which, from observations, takes on average the value of 0.07. This leads to slightly higher elevations than the second-order approximation: the mean increase is quantified as + 0.4%, or + 0.02 m. This result confirms Fedele et al. (2017) conclusion that skewness effects on crest heights are dominant compared to bound kurtosis contributions, and statistical predictions can be based on second-order models, as we have assumed in our study.

From this comparison analysis, we can conclude that, once scaled with the sea severity, the combination of numerical model directional spectrum parameters and theoretical models for spatio-temporal maximum waves provided a reliable assessment of the entity of the largest waves that occurred during the tropical storm Kong-rey in the vicinity of GORS. We shall use this positive mark to generalize the results in the East China Sea and the Yellow Sea in the remainder of this paper.

3.6.2. Large-scale analysis

The maximum wave statistics is here investigated at a large scale for the oceanic regions enclosed by the East China and Yellow Seas. At first, we approach the analysis by considering the geographical pattern of the two heights $\overline{C}_{\max}$ and $\overline{H}_{\max}$ over a cuboid 3D domain $[0, X] \times [0, Y] \times [0, D]$ of size $V = XYD = 100$ m $\times$ 100 m $\times$ 1200 s. Without loss of generality, it may represent the typical size of an offshore platform and the standard temporal sampling period for wave observations (for instance, from buoys; World Meteorological Organization, 2018). Results are illustrated in Fig. 11 for the three instants of 5 October 2018 at 04 UTC

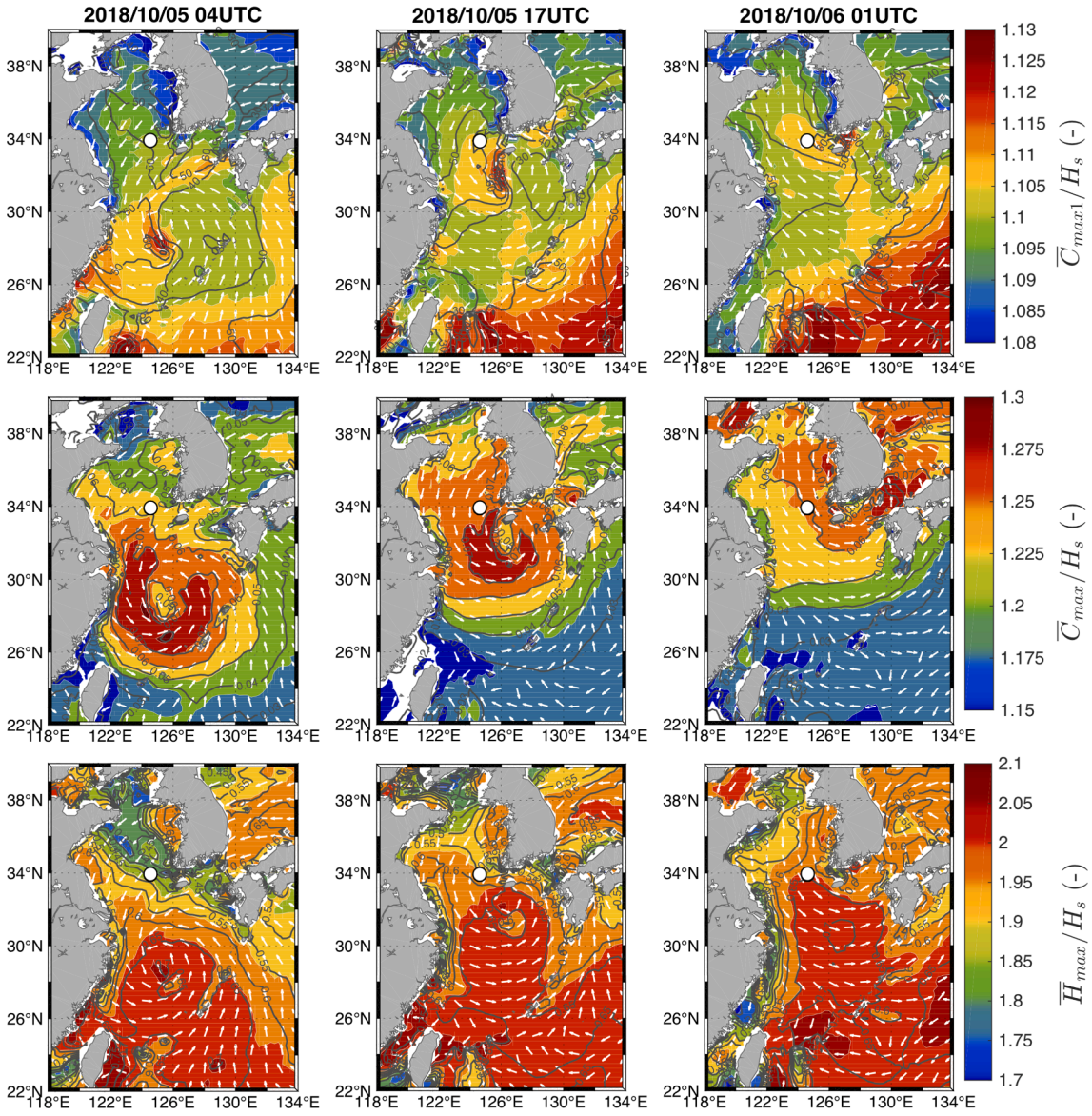

Fig. 12. Normalized (with H_s) maximum waves in the East China and Yellow Seas on 5 October 2018 at 04 UTC (left), on 5 October 2018 at 17 UTC (middle), and on 6 October 2018 at 01 UTC (right). Sea-state dependent variable-size domain Γ for spatio-temporal extreme waves: $X = L_x$, $Y = L_y$, $D = 100T_z$. Normalized linear (top) and nonlinear (middle) maximum sea surface elevation (crest height) $\overline{C}_{max1}$ and $\overline{C}_{max}$, and (bottom) maximum sea wave height $\overline{H}_{max}$ (coloured shading; scale on colour bar in units of m). The position of GORS is shown with a white dot, south-west of the Korean peninsula. Black contours show the directional spreading *dspr* (top), the wave steepness μ (middle), and the bandwidth parameter $|\psi^*|$ (bottom). Arrows (decimated for graphical purposes) depict the U_{10} wind speed vector.

(left), 5 October 2018 at 17 UTC (middle), and 6 October 2018 at 01 UTC (right), as the storm moved north. The geographical pattern of $\overline{C}_{max}$ (top panels) and $\overline{H}_{max}$ (bottom panels) depicts the radial variability of the cyclonic wave field and has an asymmetry that mirrors the significant wave height (i.e., the highest values are to the front-right of the south-to-north moving eye). Values of $\overline{C}_{max}$ and $\overline{H}_{max}$ peaked at about 14 m and 22 m, respectively, on 5 October 17 UTC (wind speed above 25 m/s in that area).

We note a very weak correlation between the maximum heights and the wave field steepness μ (contour black lines in top panels) and bandwidth parameter $|\psi^*|$ (black contour lines in bottom panels). In particular, on 5 October at 04 UTC (left panels), the steepness μ showed a radial pattern around the eye and experienced the largest values (~0.07) in the south/south-west of the eye, and it was as low as 0.05 close to the cyclone's centre. Steepness values above about 0.05 indicate that within about 400 km from the eye, the wave field follows nonlinear theory and maximum crest heights are enhanced, while at larger distances, the linear constructive interference might suffice for the description of the spatio-temporal maximum wave occurrence. The geographical pattern of $|\psi^*|$ is different from that of μ. A ridge of high bandwidth $|\psi^*|$ values (depicting narrow frequency spectra) is apparent around the eye (values from 0.65 to 0.70), then spectra broadened radially (values<0.65), experiencing stronger gradients towards the north (where following and crossing swell conditions prevail). Approaching the cyclone's landfall on 5 October at 17 UTC (middle panels), the fields were distorted by the interaction of wind and waves with the coast on three sides. Still, maximum waves remained sustained over a wide region due to the intense winds following the northward trajectory of the storm. At about the landfall time (6 October at 01 UTC, right panels), wave heights weakened with the wind, and the highest waves channelled in the Korea Strait ($\overline{C}_{max}$ and $\overline{H}_{max}$ of about 12 m and 18 m, respectively).

The geographical pattern of maximum waves, as it has been depicted in Fig. 11, changes altogether if the extreme value analysis is made over

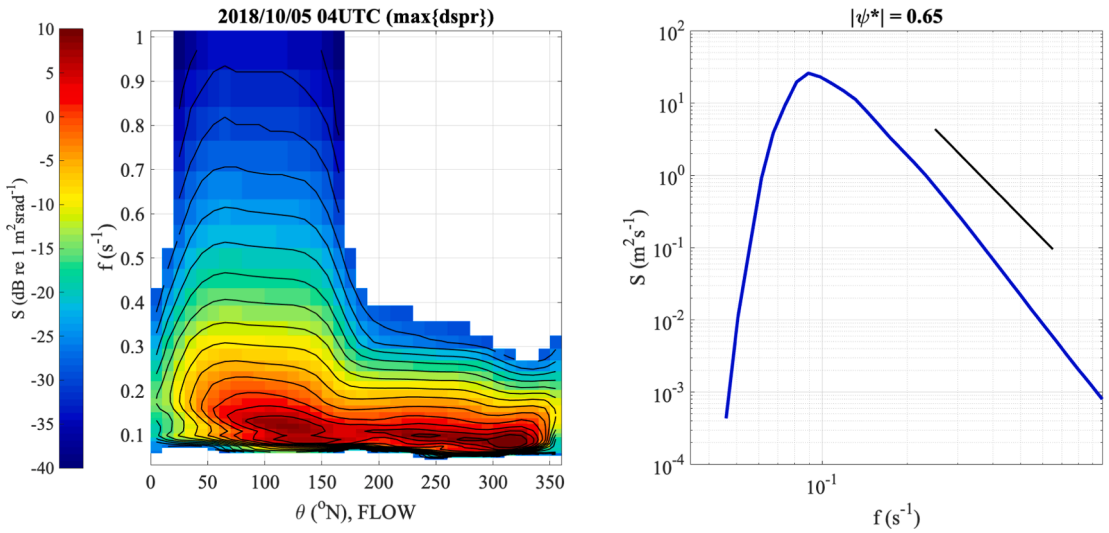

Fig. 13. (left) Frequency/direction wave spectrum $S(f, \theta)$ on 5 October at 04 UTC at the geographical point of coordinates (27.75°N, 125.25°E) where the directional spread was the largest: $dspr = 75°$. The angular separation between peaks of swell (315°N) and wind-sea (115°N) is 200°. (right) Omni-directional frequency spectrum $S(f)$. The solid black line depicts the reference slope proportional to f^{-4}.

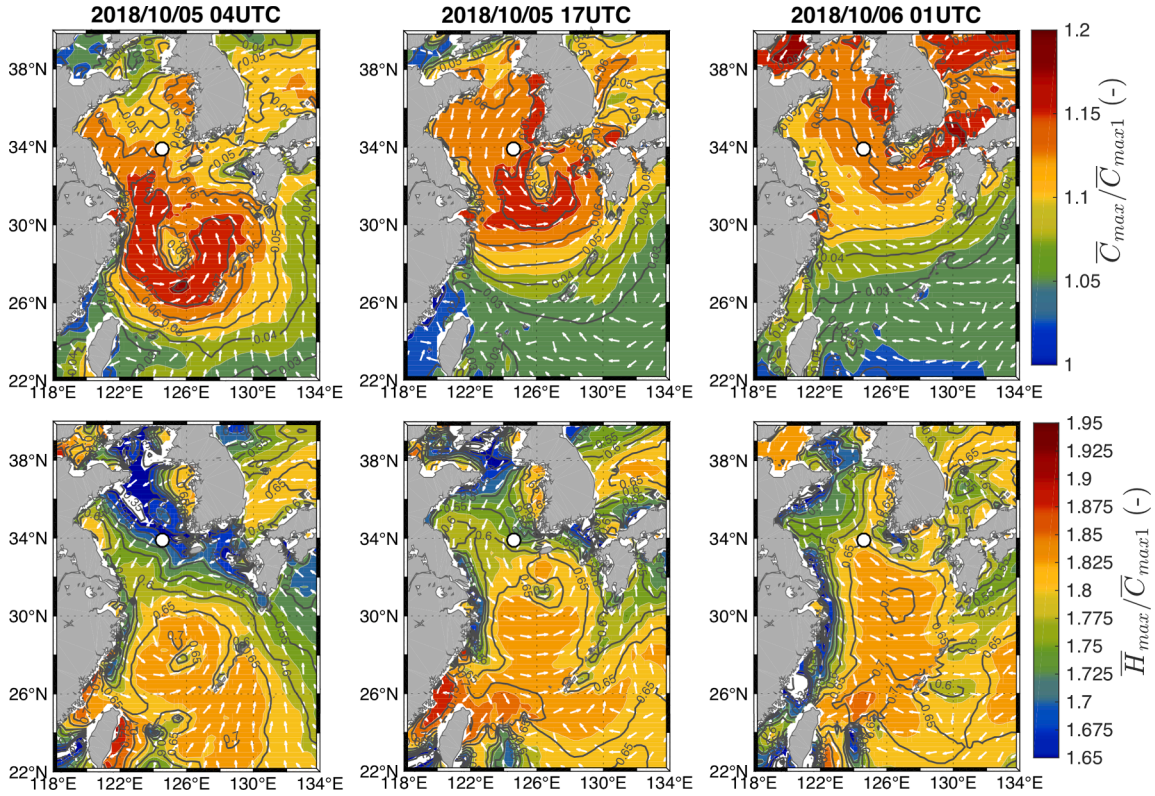

Fig. 14. Effects of second-order nonlinear bound interactions and of broad-band sea states on the maximum wave statistics in the East China and Yellow Seas on 5 October 2018 at 04 UTC (left), on 5 October at 17 UTC (middle), and on 6 October at 01 UTC (right). (top) Values of the ratio R_{NL} (coloured shading) between second-order nonlinear $\overline{C}_{max}$ and linear $\overline{C}_{max1}$ maximum sea surface elevation. The position of GORS is shown with a white dot, south-west of the Korean peninsula. Black contours show the wave steepness μ. Arrows (decimated for graphical purposes) depict the U_{10} wind speed vector. (bottom) Values of the ratio R_B (coloured shading) between wave height $\overline{H}_{max}$ and linear maximum sea surface elevation $\overline{C}_{max1}$. Black contours show the bandwidth parameter $|\psi^*|$.

a spatio-temporal domain of variable size and the expectations $\overline{C}_{max}$ and $\overline{H}_{max}$ are normalized with the significant wave height. Here, we have imposed in Eq. (3) the wave-scaled values $X = L_x$, $Y = L_y$, and $D = 100T_z$, to include only one wave, on average, in the physical xy-space. As such, the 3D *sample size* for extremes is proportional to the sea state 3D width, i.e., $N_{3D} = 100A$. This choice permits to target the directional spread effect on maximum waves, which is evaluated by removing the nonlinear effects from the crest height statistics, thus computing the Gaussian limit of $\overline{C}_{max}$ (taken by setting null the wave steepness μ), which we denote as

$$\overline{C}_{max1} = H_s\, f_{Cmax}(N_{3D},\ \mu = 0) \tag{25}$$

We note that for sea-state dependent 2D space XY and time interval D, the normalized heights $\overline{C}_{max1}/H_s$, $\overline{C}_{max}/H_s$ and $\overline{H}_{max}/H_s$ follow closely

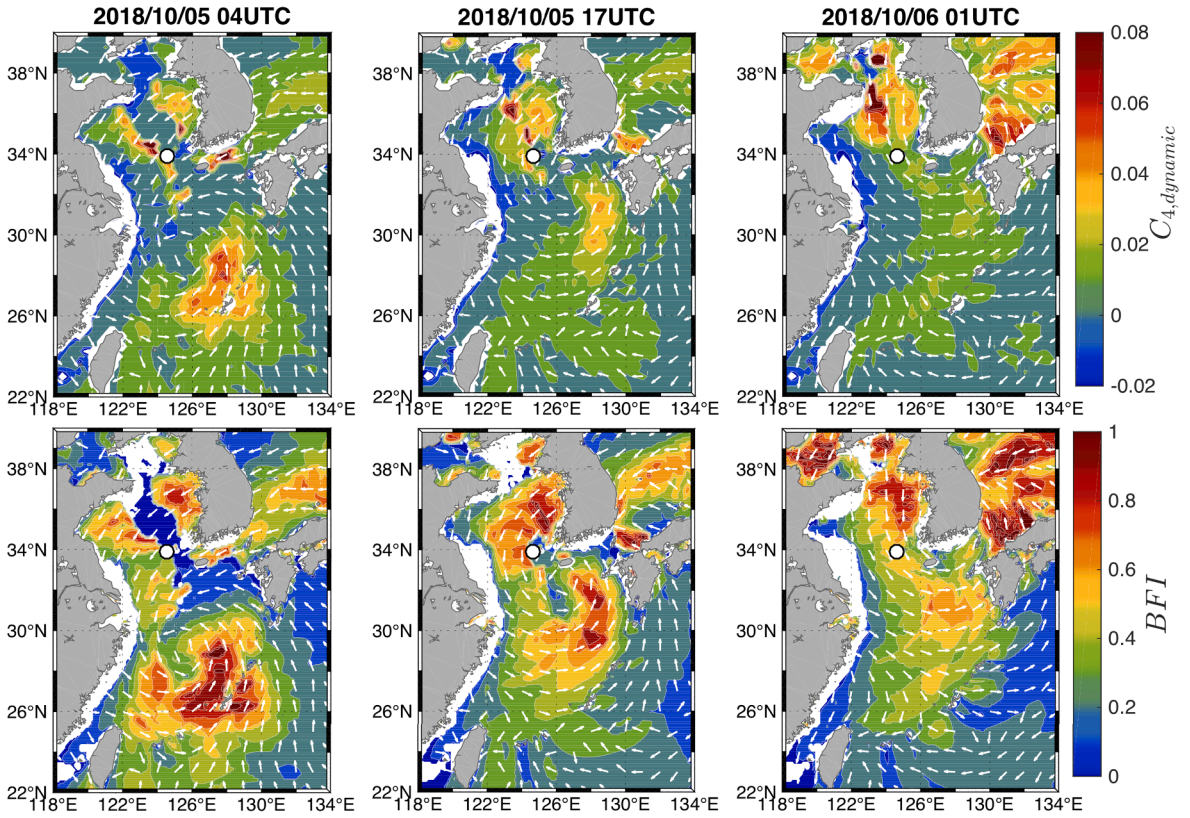

Fig. 15. Effects of nonlinear four-wave interactions on the maximum wave statistics. Maximum of the dynamic excess kurtosis $C_{4,\mathrm{dynamic}}$ (top; coloured shading, dimensionless) and Benjamin-Feir index *BFI* (bottom; coloured shading, dimensionless) in the East China and Yellow Seas on 5 October 2018 at 04 UTC (left), on 5 October at 17 UTC (middle), and on 6 October at 01 UTC (right). Arrows (decimated for graphical purposes) depict the U_{10} wind speed vector.

the geographical pattern of *dspr*, μ and $|\psi^*|$, respectively, as it is shown in Fig. 12, for the same moments as above. Sea states with large directional spread (*dspr* above 60°) leave the storm centre to north-east (as in the study of Mori, 2012), and they identify regions where the linear approximation of the maximum sea surface elevation is the highest ($\overline{C}_{\mathrm{max1}} = 1.13H_{\mathrm{s}}$ at most on 05 October at 04 UTC; top panels). There, opposing swell conditions dominate (see the directional spectrum depicted in Fig. 13), which maximize the directional spread (*dspr* = 75°) and the spatio-temporal 3D width parameter ($A = 0.86$). The steepness of 0.06 also indicates a substantial contribution from second-order nonlinearities. In the area around the cyclone, maximum nonlinear crest heights reach $\overline{C}_{\mathrm{max}} = 1.3H_{\mathrm{s}}$ and have a pattern that embraces the rear of the cyclone centre from the south-west (middle panels), whilst smaller values characterize the regions north-east of the storm. As for $\overline{H}_{\mathrm{max}}$, values higher than $2H_{\mathrm{s}}$ are likely over the whole sea region in the rear of the eye (bottom panels of Fig. 12), where the frequency spectrum is narrower ($|\psi^*| > 0.65$; see the single-peaked frequency spectrum in the right panel of Fig. 13) than in other areas. Smaller heights ($\overline{H}_{\mathrm{max}} \sim 1.8H_{\mathrm{s}}$) characterize the coastal regions.

The enhancement of crest heights by second-order nonlinear bound harmonic waves is predicted by computing the ratio

$$\begin{aligned} R_{\mathrm{NL}} &= \overline{C}_{\mathrm{max}} \Big/ \overline{C}_{\mathrm{max1}} \\ &= f_{\mathrm{Cmax}}(N_{\mathrm{3D}},\ \mu)/f_{\mathrm{Cmax}}(N_{\mathrm{3D}},\ \mu = 0) \end{aligned} \tag{26}$$

between the nonlinear and linear expected values of maximum crest heights. Fig. 14 (top panels) shows that nonlinear bound effects are small ($R_{\mathrm{NL}} < 1.05$) in the regions with mild winds far south of the storm centre, while enhancements are large ($R_{\mathrm{NL}} > 1.15$) around the storm centre where the wave steepness reached the highest values.

As for the effect of a finite bandwidth of the frequency spectral density, it is considered by noting that the function in Eq. (2) can be rewritten as follows:

$$\begin{aligned} \overline{H}_{\mathrm{max}} &= H_{\mathrm{s}}\, f_{\mathrm{Hmax}}(N_{\mathrm{3D}},\ \psi^*) \\ &= H_{\mathrm{s}}\, f_{\mathrm{Cmax}}(N_{\mathrm{3D}},\ \mu = 0) f_{\psi}(\psi^*) \end{aligned} \tag{27}$$

that can be simplified as the ratio $R_{\mathrm{B}} = \overline{H}_{\mathrm{max}}/\overline{C}_{\mathrm{max1}}$ (bottom panels of Fig. 14). During Kong-rey, values of R_{B} were in excess of 1.8 over a wide area around the storm's eye (radius as large as 400 km, stretched southward), with strong gradients near the coasts, where the bandwidth effects produced maximum wave heights that decrease rapidly (R_{B} around 1.7).

To complete the analysis, it is worth inspecting what might have been the sea regions where maximum waves heights triggered by third-order nonlinear four-wave interactions were the highest (Mori and Janssen, 2006). Accordingly, the expectation value of maximum envelope height scales with the function *f*[C_4(*BFI*, *directional width*), *sample size*], where the Benjamin-Feir index *BFI* (Janssen et al., 2003) is given by (ECMWF, 2018)

$$BFI = \frac{\epsilon\sqrt{2}}{\delta_{\omega}} \tag{28}$$

with $\epsilon = k_{\mathrm{p}}\sqrt{m_{000}}$ the integral steepness parameter (k_{p} is the peak wavenumber) and δ_{ω} the relative width of the frequency spectrum. The total excess kurtosis C_4 includes a dynamic component $C_{4,\mathrm{dynamic}}$, due to third-order quasi-resonant four-wave interactions, and a bound contribution, induced by second-order and third-order bound nonlinear interactions (Fedele, 2015). While maximum of $C_{4,\mathrm{dynamic}}$ increases with *BFI*, a finite *directional width* has the effect to give a reduction in kurtosis $C_{4,\mathrm{dynamic}}$, which tends monotonically to zero as wave energy spreads directionally (Fedele et al., 2016; Waseda et al., 2009). Therefore, the occurrence of high waves triggered by nonlinear four-wave interactions is large for sea states that exhibit steep slopes and narrow frequency and

directional bandwidths.

For typical cyclones, Mori (2012) found that the *BFI*-related largest waves are likely to occur in the south-east quadrant of the storm's eye (northern hemisphere), where *BFI* reaches the highest values and the directional spread is relatively small. An analogous analysis during Kong-rey (Fig. 15) highlights that at different storm stages, a ridge of high $C_{4,\mathrm{dynamic}}$ and *BFI* values extends east/south-east from the eye, with values of the latter that exceed 0.8 in that area. In the other quadrants around the eye, the effect of nonlinear four-wave focusing was largely reduced by the spectral broadening.

4. Concluding remarks

In this study, open-sea measurements of the 3D wave elevation field and spectral-wave model numerical simulations have been used to obtain insights into the short-term/range statistics of maximum waves under cyclone winds (northern hemisphere). We advanced previous investigations on this topic by using, for the first time, spatio-temporal extreme value formulations, which proved to be able to describe the likelihood and amplitude of maximum waves in short-crested, mixed (wind-sea and swell) sea conditions. As a matter of fact, spatio-temporal extremes allow for accounting for the angular spread between swell and wind-sea, a typical condition that occurs under rotating winds. We focused the analysis on the Northwestern Pacific during the tropical storm Kong-rey (2018) when a set of stereo observations of 3D wave fields was available in the South Yellow Sea. We performed a comparison between measurements and model estimations of wave maxima and of sea state bulk parameters, which may point to favourable conditions for the occurrence of high, individual waves. Extreme value analyses have been made over a 3D (2D space + time) domain of different characteristics to disentangle the principal mechanism responsible for generating large waves in realistic ocean seas. We remark, finally, that our results may be generalized to crossing waves in non-cyclonic conditions, which can be dangerous to ship navigation (Toffoli et al., 2005). To summarize some of the key achievements and findings of our study:

- The highest individual waves were generated to the north-east of the Kong-rey's eye, where waves remained in a region of extended fetch and propagated in approximately the same direction as the winds. This resulted in energetic sea states and higher H_s, and, consequently, $H_{\max}$ and $C_{\max}$ than those in other areas. This feature is common to typhoon and hurricanes and has general application to both spatio-temporal and temporal extremes (a particular case for $X = Y = 0$). Under Kong-rey winds in the Yellow and East China Seas, we found average $\overline{H}_{\max}$ and $\overline{C}_{\max}$ values that peaked at 22 m and 14 m, respectively. The highest waves followed the storm closely, and after its landfall, maximum heights over 10 m were simulated near the coast in the Korea Strait.
- The comparison, albeit at a single location and for a few cases, of wave maxima and sea state parameters between observations and spectral wave model results (from IFS-ECMWF) proved the capability of state-of-the-art high-resolution, coupled modelling systems to provide reliable directional wave spectrum parameters under bimodal, cyclonic conditions. The mean steepness and the geometry of the 3D wave field were estimated with good accuracy from the higher-order moments of the wave spectrum. This led to a fair estimation of the wave maximum heights.
- Apart from the wind forcing, the short-scale interaction (dispersive and directional focusing enhanced by nonlinearities up to the second order) of co-existing wind-sea and swell appears to be a mechanism for the enhanced probability of high waves. As largely discussed in the literature, and not only for cyclones, the angle of crossing between wave systems has a significant effect; in this respect, we found that where wind-sea and swell oppose, normalized extreme heights $H_{\max}/H_s$ and $C_{\max}/H_s$ are maximized as far as spatio-temporal extremes are concerned. For typical cyclone wind conditions, this situation appears to the south/south-west of the translating storm. Here, the reshaping of the bimodal nonlinear wave evolution and spectral width can make spatio-temporal extreme and rogue waves more likely.
- The novel results presented in our study complement the finding by Mori (2012) that extreme and rogue waves resulting from nonlinear four-wave interactions of long-crested waves have a greater potential of occurring in the east/south-east of typhoons (where *BFI* and dynamic excess kurtosis are maximum) than in the other quadrants. Our results and Mori's (2012) ground on competing physical mechanisms and on different spatio-temporal scales for interactions, which will eventually lead to the formation of high waves. Indeed, typical oceanic wind seas are short-crested, and wave energy can spread directionally. As a result, the enhancement of extreme waves as represented by nonlinear four-wave interactions is largely diminished, while, on the other hand, the spatio-temporal probability of high waves is increased in short-crested, multidirectional sea states. Anyhow, the role of bound-wave nonlinearities and spectral width in the distributions of maximum crest and wave heights, respectively, cannot be neglected.

Having stated the findings and limitations of the present study, we think it might be helpful to pursue the following for future research to improve the performance of extreme value models in multimodal sea states:

- Although the theoretical framework proposed in the present study confirmed its capability to describe the extreme wave statistics in short-crested seas, a more extensive data set should be collected in different cyclone conditions (e.g., for the translation speed) and wave characteristics (e.g., for swell dominated seas) to be compared with theoretical and numerical model predictions to gain further insights into which physical mechanisms might be behind the extreme wave generation in different regions around the cyclone.
- For extreme wave analysis, mixed sea states, combination of wind-sea and swell, should be partitioned (see e.g., Trulsen et al., 2015), and the short-term/range statistical analysis be performed on each partition separately. This separation will allow us to better interpret the nonlinear extreme value statistics, on the one hand, of each wave system and, on the other, of the interacting modes (see e.g., McAllister et al., 2019).

Funding

The work was supported by the project "Establishment of the ocean research station in the jurisdiction zone and convergence research", funded by the Ministry of Oceans and Fisheries, Republic of Korea. JY also appreciate partial funding of KIOST (PE99842) and AB by the Copernicus Marine Environment Monitoring Service (CMEMS) LATEMAR project. CMEMS is implemented by Mercator Ocean in the framework of a delegation agreement with the European Union. This work has also been conducted as part of the bilateral project EOLO-1 ("Extreme Oceanic waves during tropical, tropical-like, and bomb cyclones") between CNR-ISMAR and the University of Tokyo (Japan; Prof. Takuji Waseda).

CRediT authorship contribution statement

Alvise Benetazzo: Conceptualization, Methodology, Formal analysis, Data curation, Supervision, Project administration, Funding acquisition. **Francesco Barbariol:** Software, Formal analysis, Investigation, Funding acquisition. **Filippo Bergamasco:** Software, Investigation. **Luciana Bertotti:** Investigation. **Jeseon Yoo:** Resources, Data curation. **Jae-Seol Shim:** Resources. **Luigi Cavaleri:** Investigation.

Declaration of Competing Interest

The authors declare that they have no known competing financial interests or personal relationships that could have appeared to influence the work reported in this paper.

Acknowledgements

We are grateful to Prof. Miguel Onorato and Dr Silvio Davison for their advice on the statistics of multimodal sea states, and Prof. Antonio Ricchi for the fruitful discussions about atmospheric cyclones.

Appendix A. Wave spectra from 3D stereo data

For each stereo record of the surface elevation field $\eta(x, y, t)$, the 3D wavenumber/frequency spectrum $S(k_x, k_y, f_a)$ was obtained from the Fourier transform pair in the following vector form

$$Z(k_x, k_y, \omega_a) = \int_t \int_x \eta(x, y, t) e^{i(\boldsymbol{k}\cdot\boldsymbol{x} - \omega_a t)} d\boldsymbol{x} dt \tag{A.1}$$

where $\omega_a = 2\pi f_a$ is the absolute angular frequency. The variance of spectral estimates has been reduced by averaging, following the Welch's method (Welch, 1967) over four segments of equal length in time and 50% overlap, covering the surface window of sides of 55.5 m (y-axis) and 70.5 m (x-axis). The 3D elevation data have been tapered with a Hanning window of the same size to suppress the side-lobe leakage.

Since the sea region around GORS is exposed to large tidal and wind-driven currents, their contribution was taken into account to correct the shape of $S(k_x, k_y, f_a)$ (Benetazzo et al., 2018a). Indeed, in the presence of a sea current, the energies of linear and nonlinear wave harmonics in the 3D spectral space are shifted (Fig. A1), and for a given wavenumber $\boldsymbol{k}$, the absolute wave frequency f_a that is perceived by a fixed observer is different from the intrinsic (or relative) frequency f that is seen by an observer moving with the current. Indeed, the Doppler effect modifies the observed frequency of each elementary periodic wave that makes up the random sea (Lindgren et al., 1999).

For harmonic waves in the limit of small wave steepness and neglecting the modulation of short waves by long waves (Longuet-Higgins and Stewart, 1960), the relation between f_a and f is given by the following formula (Stewart and Joy, 1974):

$$\begin{aligned} &2\pi f_a - 2\pi f - \boldsymbol{k}\cdot\boldsymbol{U} \\ &= 2\pi f_a - 2\pi f - kU\cos(\theta - \theta_U) = 0 \end{aligned} \tag{A.2}$$

where $\boldsymbol{U}$ is the medium velocity vector (of direction θ_U). At the leading order, it is assumed that the dispersion relationship of the linear wave theory provides a unique relationship between the frequency f and the wavenumber k as follows:

$$\omega = 2\pi f = \sqrt{gk\tanh(kd)} \tag{A3}$$

where g is the acceleration due to the gravity force. At any depth d, the effective current $\boldsymbol{U}$ in Eq. (A.2) is a function of k, that is, $\boldsymbol{U} = \boldsymbol{U}(k)$, since harmonic waves with wavenumber k can be considered to feel the current integrated from the surface up to the depth $\sim 1/k$ (Kirby and Chen, 1989; Stewart and Joy, 1974).

Since the spectral representation in absolute frequencies experiences a shifting of the energy, we used the (k_x, k_y, f_a) spectral information to evaluate the velocity vector, whose speed U varied from 0.2 to 0.8 m/s during the wave observations from GORS on 5 and 6 October 2018. We then mapped the 3D Fourier components of $S(k_x, k_y, f_a)$ from the absolute frequency (k_x, k_y, f_a)-space to the intrinsic frequency (k_x, k_y, f)-space as follows:

$$S(k_x, k_y, f) = S(k_x, k_y, f_a)|df_a/df| \tag{A4}$$

where $J = |df_a / df|$ is the Jacobian of the transformation, which in deep water is given by

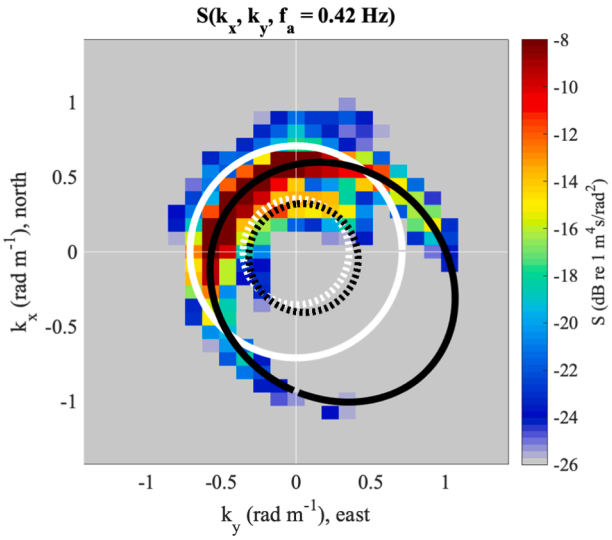

Fig. A1. 2D wavenumber spectrum $S(k_x, k_y)$ taken at the absolute frequency $f_a = 0.44$ Hz from the 3D wavenumber/frequency spectrum $S(k_x, k_y, f_a)$. Stereo data from GORS on 6 October 2018 at 05 UTC. Energy appears in the direction where it is coming from (330°N, on average), and the x- and y-axis are mapped as in the WASS reference system. The solid white and black lines show the linear dispersion relation in still water and in the presence of a near-surface uniform current (estimated with speed $U = 0.65$ m/s), respectively. The dotted white and black lines show the dispersion relation of the positive interaction terms of the second-order nonlinear bound harmonic waves in still water and in the presence of a near-surface uniform current, respectively.

$$J = |1 + (4\pi/g)fU\cos(\theta - \theta_U)| \quad \text{(A5)}$$

Finally, the relative-frequency 1D spectrum $S(f)$ was obtained by integration of $S(k_x, k_y, f)$ over the 2D wavenumber (k_x, k_y)-space, and it was used for the estimation of the wave parameters μ and ψ^* from the observations (Table 1).

References

Adler, R.J., 2000. On excursion sets, tube formulas and maxima of random fields. Ann. Appl. Probab. 10, 1–74. https://doi.org/10.1214/aoap/1019737664.

Adler, R.J., 1981. The Geometry of Random Fields. John Wiley, New York (USA), p. 302.

Barbariol, F., Alves, J.-H., Benetazzo, A., Bergamasco, F., Bertotti, L., Carniel, S., Cavaleri, L., Y. Chao, Y., Chawla, A., Ricchi, A., Sclavo, M., Tolman, H., 2017. Numerical Modeling of Space-Time Wave Extremes using WAVEWATCH III. Ocean Dyn. 67 (3-4), 535–549. https://doi.org/10.1007/s10236-016-1025-0.

Barbariol, F., Bidlot, J.-R., Cavaleri, L., Sclavo, M., Thomson, J., Benetazzo, A., 2019. Maximum wave heights from global model reanalysis. Prog. Oceanogr. 175, 139–160. https://doi.org/10.1016/j.pocean.2019.03.009.

Baxevani, A., Rychlik, I., 2006. Maxima for Gaussian seas. Ocean Eng. 33 (7), 895–911. https://doi.org/10.1016/j.oceaneng.2005.06.006.

Benetazzo, A., 2006. Measurements of short water waves using stereo matched image sequences. Coast. Eng. 53 (12), 1013–1032. https://doi.org/10.1016/j.coastaleng.2006.06.012.

Benetazzo, A., Ardhuin, F., Bergamasco, F., Cavaleri, L., Guimaraes, L., Schwendeman, M., Sclavo, M., Thomson, J., Torsello, A., 2017a. On the shape and likelihood of oceanic rogue waves. Sci. Rep. 7 (8276), 1–11. https://doi.org/10.1038/s41598-017-07704-9.

Benetazzo, A., Barbariol, F., Bergamasco, F., Sandro, C., Sclavo, M., Yoo, J., Cavaleri, L., Kim, S.S., Bertotti, L., Barbariol, F., Shim, J.S., 2017b. Space-time extreme wind waves: Analysis and prediction of shape and height. Ocean Model. 113, 201–216. https://doi.org/10.1016/j.ocemod.2017.03.010.

Benetazzo, A., Barbariol, F., Bergamasco, F., Torsello, A., Carniel, S., Sclavo, M., 2015. Observation of extreme sea waves in a space-time ensemble. J. Phys. Oceanogr. 45, 2261–2275. https://doi.org/10.1175/JPO-D-15-0017.1.

Benetazzo, A., Barbariol, F., Davison, S., 2020. Short-Term/Range Extreme-Value Probability Distributions of Upper Bounded Space-Time Maximum Ocean Waves. J. Mar. Sci. Eng. 8, 1–14. https://doi.org/10.3390/JMSE8090679.

Benetazzo, A., Barbariol, F., Pezzutto, P., Staneva, J., Behrens, A., Davison, S., Bergamasco, F., Sclavo, M., Cavaleri, L., 2021. Towards a unified framework for extreme sea waves from spectral models: rationale and applications. Ocean Eng. 219, 108263. https://doi.org/10.1016/j.oceaneng.2020.108263.

Benetazzo, A., Bergamasco, F., Yoo, J., Cavaleri, L., Kim, S.S., Bertotti, L., Barbariol, F., Shim, J.S., 2018a. Characterizing the signature of a spatio-temporal wind wave field. Ocean Model. 129, 104–123. https://doi.org/10.1016/j.ocemod.2018.06.007.

Benetazzo, A., Fedele, F., Gallego, G., Shih, P.-C., Yezzi, A., 2012. Offshore stereo measurements of gravity waves. Coast. Eng. 64, 127–138. https://doi.org/10.1016/j.coastaleng.2012.01.007.

Benetazzo, A., Serafino, F., Bergamasco, F., Ludeno, G., Ardhuin, F., Sutherland, P., Sclavo, M., Barbariol, F., 2018b. Stereo imaging and X-band radar wave data fusion: An assessment. Ocean Eng. 152, 346–352. https://doi.org/10.1016/j.oceaneng.2018.01.077.

Benjamin, T.B., Feir, J.E., 1967. The disintegration of wave trains on deep water Part 1. Theory. J. Fluid Mech. 27 (3), 417–430.

Bergamasco, F., Torsello, A., Sclavo, M., Barbariol, F., Benetazzo, A., 2017. WASS: An open-source pipeline for 3D stereo reconstruction of ocean waves. Comput. Geosci. 107, 28–36. https://doi.org/10.1016/j.cageo.2017.07.001.

Bitner-Gregersen, E.M., Gramstad, O., 2015. ROGUE WAVES. Impact on ships and offshore structures. DNV GL STRATEGIC RESEARCH & INNOVATION POSITION PAPER 05–2015.

Black, P.G., D'Asaro, E.A., Drennan, W.M., French, J.R., Niiler, P.P., Sanford, T.B., Terrill, E.J., Walsh, E.J., Zhang, J.A., 2007. Air-Sea Exchange in Hurricanes: Synthesis of Observations from the Coupled Boundary Layer Air-Sea Transfer Experiment. Bull. Am. Meteorol. Soc. 88, 357–374. https://doi.org/10.1175/BAMS-88-3-357.

Boccotti, P., 2000. Wave Mechanics for Ocean Engineering. Elsevier Science B.V., 496 pp.

Cardone, V.J., Cox, A.T., 2009. Tropical cyclone wind field forcing for surge models: critical issues and sensitivities. Nat. Hazards 51 (1), 29–47. https://doi.org/10.1007/s11069-009-9369-0.

Casas-Prat, M., Holthuijsen, L.H., 2010. Short-term statistics of waves observed in deep water. J. Geophys. Res. 115, C09024. https://doi.org/10.1029/2009JC005742.

Cavaleri, L., Alves, J.H.G.M., Ardhuin, F., Babanin, A., Banner, M., Belibassakis, K., Benoit, M., Donelan, M., Groeneweg, J., Herbers, T.H.C., Hwang, P., Janssen, P.A.E.M., Janssen, T., Lavrenov, I. V., Magne, R., Monbaliu, J., Onorato, M., Polnikov, V., Resio, D., Rogers, W.E., Sheremet, A., McKee Smith, J., Tolman, H.L., van Vledder, G., Wolf, J., Young, I., 2007. Wave modelling - The state of the art. Prog. Oceanogr. doi:10.1016/j.pocean.2007.05.005.

Cavaleri, L., Barbariol, F., Benetazzo, A., 2020. Wind-Wave Modeling: Where We Are, Where to Go. J. Mar. Sci. Eng. 8, 260. https://doi.org/10.3390/jmse8040260.

Cavaleri, L., Barbariol, F., Benetazzo, A., Bertotti, L., Bidlot, J.-R., Janssen, P., Wedi, N., 2016. The Draupner wave: A fresh look and the emerging view. J. Geophys. Res. Ocean. 121 (8), 6061–6075. https://doi.org/10.1002/2016JC011649.

Cavaleri, L., Benetazzo, A., Barbariol, F., Bidlot, J.-R.-J., Janssen, P.A.E.M., 2017. The Draupner event: the large wave and the emerging view. Bull. Am. Meteorol. Soc. 98, 729–735. https://doi.org/10.1175/BAMS-D-15-00300.1.

Cavaleri, L., Bertotti, L., Torrisi, L., Bitner-Gregersen, E., Serio, M., Onorato, M., 2012. Rogue waves in crossing seas: The Louis Majesty accident. J. Geophys. Res. Ocean. 117 (C11), n/a–n/a. https://doi.org/10.1029/2012JC007923.

Dematteis, G., Grafke, T., Onorato, M., Vanden-Eijnden, E., 2019. Experimental Evidence of Hydrodynamic Instantons: The Universal Route to Rogue Waves. Phys. Rev. X 9, 041057. https://doi.org/10.1103/PhysRevX.9.041057.

Didenkulova, E., 2020. Catalogue of rogue waves occurred in the World Ocean from 2011 to 2018 reported by mass media sources. Ocean Coast. Manag. 188, 105076. https://doi.org/10.1016/j.ocecoaman.2019.105076.

Gl, D.N.V., 2017. DNVGL-RP-C205: Environmental Conditions and Environmental Loads. DNV GL Recommended Practice (August) 1–259.

Donelan, M.A., Magnusson, A.-K., 2017. The Making of the Andrea Wave and other Rogues. Sci. Rep. 7, 44124. https://doi.org/10.1038/srep44124.

Draper, L., 1964. "Freak" ocean waves. Oceanus 10, 13–15.

Dysthe, K., Krogstad, H.E., Müller, P., 2008. Oceanic Rogue Waves. Annu. Rev. Fluid Mech. 40 (1), 287–310. https://doi.org/10.1146/annurev.fluid.40.111406.102203.

ECMWF, 2018. Part VII : ECMWF Wave Model. IFS Documentation CY45R1.

Fedele, F., 2015. On the kurtosis of ocean waves in deep water. J. Fluid Mech. 782, 25–36.

Fedele, F., 2012. Space-Time Extremes in Short-Crested Storm Seas. J. Phys. Oceanogr. 42, 1601–1615. https://doi.org/10.1175/JPO-D-11-0179.1.

Fedele, F., Banner, M.L., Barthelemy, X., 2020. Crest speeds of unsteady surface water waves. J. Fluid Mech. 899, A5. https://doi.org/10.1017/jfm.2020.424.

Fedele, F., Benetazzo, A., Gallego, G., Shih, P.-C., Yezzi, A., Barbariol, F., Ardhuin, F., 2013. Space–time measurements of oceanic sea states. Ocean Model. 70, 103–115. https://doi.org/10.1016/j.ocemod.2013.01.001.

Fedele, F., Brennan, J., Sonia Ponce de León, Dudley, J., Dias, F., 2016. Real world ocean rogue waves explained without the modulational instability. Sci. Rep. 6, 1–11.

Fedele, Francesco, Gallego, Guillermo, Yezzi, Anthony, Benetazzo, Alvise, Cavaleri, Luigi, Sclavo, Mauro, Bastianini, Mauro, 2012. Euler characteristics of oceanic sea states. Math. Comput. Simul. 82 (6), 1102–1111. https://doi.org/10.1016/j.matcom.2011.05.009.

Fedele, F., Lugni, C., Chawla, A., 2017. The sinking of the El Faro : predicting real world rogue waves during Hurricane Joaquin. Sci. Rep. 7 (11188), 1–15. https://doi.org/10.1038/s41598-017-11505-5.

Fedele, F., Tayfun, M.A., 2009. On nonlinear wave groups and crest statistics. J. Fluid Mech. 620, 221–239. https://doi.org/10.1017/S0022112008004424.

Fu, Dongyang, Luan, Hong, Pan, Delu, Zhang, Ying, Wang, Li'an, Liu, Dazhao, Ding, Youzhuan, Li, Xue, 2016. Impact of two typhoons on the marine environment in the Yellow Sea and East China Sea. Chinese J. Oceanol. Limnol. 34 (4), 871–884. https://doi.org/10.1007/s00343-016-5049-6.

Gelci, R., Cazalé, J., Vassal, J., 1957. Prévision de la houle. La méthode des densités spectroangulaires. Bull. Inform. Com. Cent. Ocean. D'Etude Cotes 416–435.

Gemmrich, J., Garrett, C., 2011. Dynamical and statistical explanations of observed occurrence rates of rogue waves. Nat. Hazards Earth Syst. Sci. 11, 1437–1446. https://doi.org/10.5194/nhess-11-1437-2011.

Guedes Soares, C., Cherneva, Z., Antão, E.M., 2004. Abnormal waves during Hurricane Camille. J. Geophys. Res. Ocean. 109 (C8) https://doi.org/10.1029/2003JC002244.

Gumbel, E.J., 1958. Statistics of Extremes. Columbia University Press, p. 358.

Hasselmann, K., Barnett, T.P., Bouws, E., Carlson, H., Cartwright, D.E., Enke, K., Ewing, J.A., Gienapp, H., Hasselmann, D.E., Kruseman, P., Meerburg, A., Müller, P., Olbers, D.J., Richter, K., Sell, W., Walden, H., 1973. Measurements of wind-wave growth and swell decay during the Joint North Sea Wave Project (JONSWAP). Deutches Hydrogr. Inst. A8, 1–95.

Hasselmann, S., Hasselmann, K., Allender, J.H., Barnett, T.P., 1985. Computations and Parameterizations of the Nonlinear Energy Transfer in a Gravity-Wave Specturm. Part II: Parameterizations of the Nonlinear Energy Transfer for Application in Wave Models. J. Phys. Oceanogr. 15 (11), 1378–1391.

Holthuijsen, L.H., 2007. Waves in Oceanic and Coastal Waters. Cambridge University Press, p. 387.

Holthuijsen, L.H., Powell, M.D., Pietrzak, J.D., 2012. Wind and waves in extreme hurricanes. J. Geophys. Res. Ocean. 117 (C09003), 10–15. https://doi.org/10.1029/2012JC007983.

Hu, K., Chen, Q., 2011. Directional spectra of hurricane-generated waves in the Gulf of Mexico. Geophys. Res. Lett. doi:10.1029/2011GL049145.

Janssen, Peter A.E.M., 1991. Quasi-linear Theory of Wind-Wave Generation Applied to Wave Forecasting. J. Phys. Oceanogr. 21 (11), 1631–1642.

Janssen, P.A.E.M., Park, S., Kingdom, U., Janssen, P.A.E.M., 2003. Nonlinear Four-Wave Interactions and Freak Waves. J. Phys. Oceanogr. 33, 863–884. https://doi.org/10.1175/1520-0485(2003)33<863:NFIAFW>2.0.CO;2.

Jiang, Xingjie, Guan, Changlong, Wang, Daolong, 2019. Rogue waves during Typhoon Trami in the East China Sea. J. Oceanol. Limnol. 37 (6), 1817–1836. https://doi.org/10.1007/s00343-019-8256-0.

Jun, Ki Cheon, Jeong, Weon Mu, Choi, Jin Yong, Park, Kwang Soon, Jung, Kyung Tae, Kim, Mee Kyung, Chae, Jang Won, Qiao, Fangli, 2015. Simulation of the extreme waves generated by typhoon Bolaven (1215) in the East China Sea and Yellow Sea. Acta Oceanol. Sin. 34 (12), 19–28. https://doi.org/10.1007/s13131-015-0779-4.

King, D.B., Shemdin, O.H., 1978. Radar observations of hurricane wave directions. In: 16th International Confession on Coastal Engineering. Hamburg, Germany, pp. 209–226.
Kirby, James T., Chen, Tsung-Muh, 1989. Surface-waves on vertically sheared flows: approximate dispersion relations. J. Geophys. Res. Ocean. 94 (C1), 1013. https://doi.org/10.1029/JC094iC01p01013.
Komen, G.J., Cavaleri, L., M. Donelan, K.H., Hasselmann, S., Janssen, P.A.E.M., 1994. Dynamics and Modelling of Ocean Waves. Cambridge University Press.
Krogstad, H.E., Liu, J., Socquet-Juglard, H., Dysthe, K., Trulsen, K., 2004. Spatial Extreme Value Analysis Of Nonlinear Simulations Of Random Surface Waves. in: Proceedings of OMAE04 23rd International Conference on Offshore Mechanics and Arctic Engineering.
Kuik, A.J., Van Vledder, G.P., Holthuijsen, L.H., 1988. A method for routine analysis of pitch and roll buoy wave data. J. Phys. Oceanogr. https://doi.org/10.1175/1520-0485(1988)018<1020:AMFTRA>2.0.CO;2.
Leckler, F., Ardhuin, F., Peureux, C., Benetazzo, A., Bergamasco, F., Dulov, V., 2015. Analysis and interpretation of frequency-wavenumber spectra of young wind waves. J. Phys. Oceanogr. 45, 2484–2496. https://doi.org/10.1175/JPO-D-14-0237.1.
Li, S., Jiang, H., Hou, Y., Wang, N., Lu, J., 2020. Increasing Historical Tropical Cyclone-Induced Extreme Wave Heights in the Northern East China Sea during 1979 to 2018. Remote Sens. 12, 2464. https://doi.org/10.3390/rs12152464.
Lindgren, Georg, 1972. Local maxima of Gaussian Fields. Ark. Mat. 10 (1-2), 195–218.
Lindgren, G., Rychlik, I., Prevosto, M., 1999. Stochastic Doppler shift and encountered wave period distributions in Gaussian waves. Ocean Eng. 26 (6), 507–518.
Liu, Defu, Pang, Liang, Xie, Botao, 2009. Typhoon disaster in China: prediction, prevention, and mitigation. Nat. Hazards 49 (3), 421–436. https://doi.org/10.1007/s11069-008-9262-2.
Liu, Q., Babanin, A., Fan, Y., Zieger, S., Guan, C., Moon, I.-J., 2017. Numerical simulations of ocean surface waves under hurricane conditions: Assessment of existing model performance. Ocean Model. 118, 73–93. https://doi.org/10.1016/j.ocemod.2017.08.005.
Longuet-Higgins, M.S., 1975. On the joint distribution of the periods and amplitudes of sea waves. J. Geophys. Res. 80 (18), 2688–2694.
Longuet-Higgins, M.S., 1963. The effect of nonlinearities on statistical distribution in the theory of sea waves. J. Fluid Mech. 17, 459–480.
Longuet-Higgins, M.S., 1952. On the statistical distribution of the heights of sea waves. J. Mar. Res. 11, 245–265.
Longuet-Higgins, M.S., Stewart, R.W., 1960. Changes in the form of short gravity waves on long waves and tidal currents. J. Fluid Mech. 8 (04), 565. https://doi.org/10.1017/S0022112060000803.
Magnusson, A.K., Donelan, M.A., Drennan, W.M., 1999. On estimating extremes in an evolving wave field. Coast. Eng. 36 (2), 147–163. https://doi.org/10.1016/S0378-3839(99)00004-6.
Magnusson, L., Bidlot, J.-R., Bonavita, M., Brown, A.R., Browne, P.A., De Chiara, G., Dahoui, M., Lang, S.T.K., McNally, T., Mogensen, K.S., Pappenberger, F., Prates, F., Rabier, F., Richardson, D.S., Vitart, F., Malardel, S., 2019. ECMWF Activities for Improved Hurricane Forecasts. Bull. Am. Meteorol. Soc. 100, 445–458. https://doi.org/10.1175/BAMS-D-18-0044.1.
Mao, Miaohua, van der Westhuysen, André J., Xia, Meng, Schwab, David J., Chawla, Arun, 2016. Modeling wind waves from deep to shallow waters in Lake Michigan using unstructured SWAN. J. Geophys. Res. Ocean. 121 (6), 3836–3865. https://doi.org/10.1002/jgrc.v121.610.1002/2015JC011340.
McAllister, M.L., Adcock, T.A.A., Taylor, P.H., van den Bremer, T.S., 2019. A Note on the Second-Order Contribution to Extreme Waves Generated During Hurricanes. J. Offshore Mech. Arct. Eng. 141, 1–10. https://doi.org/10.1115/1.4042540.
Mendes, S., Scotti, A., 2020. Rogue wave statistics in (2+1) Gaussian seas I: Narrow-banded distribution. Appl. Ocean Res. 99, 102043. https://doi.org/10.1016/j.apor.2019.102043.
Moon, I.-J., Kim, M., Joh, M., Ahn, J., Shim, J.-S., Jung, J., 2016. Recent record-breaking high ocean waves induced by typhoons in the seas adjacent to Korea. J. Coast. Res. 75, 1397–1401. doi:10.2112/SI75-280.1.
Moon, I.J., Ginis, I., Hara, T., Tolman, H.L., Wright, C.W., Walsh, E.J., 2003. Numerical simulation of sea surface directional wave spectra under hurricane wind forcing. J. Phys. Oceanogr. doi:10.1175/2410.1.
Mori, Nobuhito, 2012. Freak waves under typhoon conditions. J. Geophys. Res. Ocean. 117 (C11), n/a–n/a. https://doi.org/10.1029/2011JC007788.
Mori, N., Janssen, P.a.E.M., 2006. On Kurtosis and Occurrence Probability of Freak Waves. J. Phys. Oceanogr. 36, 1471–1483.
Naess, Arvid, 1985. On the distribution of crest to trough wave heights. Ocean Eng 12 (3), 221–234. https://doi.org/10.1016/0029-8018(85)90014-9.
Ochi, M.K., 1998. Ocean Waves, Ocean waves: the stochastic approach. Cambridge University Press. doi:10.1017/CBO9780511529559.
Onorato, Miguel, Osborne, Alfred R., Serio, Marina, Bertone, Serena, 2001. Freak Waves in Random Oceanic Sea States. Phys. Rev. Lett. 86 (25), 5831–5834. https://doi.org/10.1103/PhysRevLett.86.5831.
Onorato, M., Proment, D., Toffoli, A., 2010. Freak waves in crossing seas. Eur. Phys. J. Spec. Top. 185 (1), 45–55. https://doi.org/10.1140/epjst/e2010-01237-8.
Onorato, M., Residori, S., Bortolozzo, U., Montina, A., Arecchi, F.T., 2013. Rogue waves and their generating mechanisms in different physical contexts. Phys. Rep. 528 (2), 47–89. https://doi.org/10.1016/j.physrep.2013.03.001.
Onorato, M., Waseda, T., Toffoli, A., Cavaleri, L., Gramstad, O., Janssen, P.A.E.M., Kinoshita, T., Monbaliu, J., Mori, N., Osborne, A.R., Serio, M., Stansberg, C.T., Tamura, H., Trulsen, K., 2009. Statistical Properties of Directional Ocean Waves: The Role of the Modulational Instability in the Formation of Extreme Events. Phys. Rev. Lett. 102, 114502 https://doi.org/10.1103/PhysRevLett.102.114502.
Peureux, C., Benetazzo, A., Ardhuin, F., 2018. Note on the directional properties of meter-scale gravity waves. Ocean Sci. 14, 41–52. https://doi.org/10.5194/os-2017-48.
Pierson, W.J., Neumann, G., James, R.W., 1955. Practical Methods for Observing and Forecasting Ocean Waves by Means of Wave Spectra and Statistics. Washington, U.S. Navy Hydrogr. Off. Publ. No. 603, 284 pp.
Piterbarg, V.I., 1996. Asymptotic Methods in the Theory of Gaussian Processes and Fields. Translations of Mathematical Monographs 206 pp.
Ponce de León, S., Guedes Soares, C., 2014. Extreme wave parameters under North Atlantic extratropical cyclones. Ocean Model. 81, 78–88. https://doi.org/10.1016/j.ocemod.2014.07.005.
Powell, Mark D., Vickery, Peter J., Reinhold, Timothy A., 2003. Reduced drag coefficient for high wind speeds in tropical cyclones. Nature 422 (6929), 279–283. https://doi.org/10.1038/nature01481.
Rodwell, M., Ferranti, L., Haiden, T., Magnusson, L., 2015. New developments in the diagnosis and verification of high-impact weather forecasts. ECMWF Tech. Memo. 759, 44 pp., www.ecmwf.int/en /elibrary/15255-new-developments-diagnosis-and-verification-high-impact-weather-forecasts.
Rogers, W.E., Van Vledder, G.P., 2013. Frequency width in predictions of windsea spectra and the role of the nonlinear solver. Ocean Model. 70, 52–61. https://doi.org/10.1016/j.ocemod.2012.11.010.
Santo, H., Taylor, P.H., Eatock Taylor, R., Choo, Y.S., 2013. Average Properties of the Largest Waves in Hurricane Camille. J. Offshore Mech. Arct. Eng. 135 https://doi.org/10.1115/1.4006930.
Slunyaev, A., Pelinovsky, E., Guedes Soares, C., 2005. Modeling freak waves from the North Sea. Appl. Ocean Res. 27 (1), 12–22. https://doi.org/10.1016/j.apor.2005.04.002.
Stewart, Robert H., Joy, Joseph W., 1974. HF radio measurements of surface currents. Deep. Res. 21 (12), 1039–1049.
Støle-Hentschel, Susanne, Trulsen, Karsten, Nieto Borge, José Carlos, Olluri, Shkurte, 2020. Extreme Wave Statistics in Combined and Partitioned Windsea and Swell. Water Waves 2 (1), 169–184. https://doi.org/10.1007/s42286-020-00026-w.
Stopa, J.E., Ardhuin, F., Babanin, A., Zieger, S., 2016. Comparison and validation of physical wave parameterizations in spectral wave models. Ocean Model. 103, 2–17. https://doi.org/10.1016/j.ocemod.2015.09.003.
Aziz Tayfun, M., 2006. Statistics of nonlinear wave crests and groups. Ocean Eng. 33 (11-12), 1589–1622. https://doi.org/10.1016/j.oceaneng.2005.10.007.
Tayfun, M.A., 1980. Narrow-band nonlinear sea waves. J. Geophys. Res. 85, 1548–1552. https://doi.org/10.1029/JC085iC03p01548.
Toffoli, A., Lefèvre, J.M., Bitner-Gregersen, E., Monbaliu, J., 2005. Towards the identification of warning criteria: Analysis of a ship accident database. Appl. Ocean Res. 27 (6), 281–291. https://doi.org/10.1016/j.apor.2006.03.003.
Tolman, H.L., 2013. A Generalized Multiple Discrete Interaction Approximation for resonant four-wave interactions in wind wave models. Ocean Model. 70, 11–24. https://doi.org/10.1016/j.ocemod.2013.02.005.
Trulsen, K., Nieto Borge, J.C., Gramstad, O., Aouf, L., Lefèvre, J., 2015. Crossing sea state and rogue wave probability during the Prestige accident. J. Geophys. Res. Ocean. 120, 7113–7136. https://doi.org/10.1002/2015JC011161.
Wada, Akiyoshi, Uehara, Tomohiro, Ishizaki, Shiro, 2014. Typhoon-induced sea surface cooling during the 2011 and 2012 typhoon seasons: observational evidence and numerical investigations of the sea surface cooling effect using typhoon simulations. Prog. Earth Planet. Sci. 1 (1), 11. https://doi.org/10.1186/2197-4284-1-11.
Wang, D.W., 2005. Extreme Waves Under Hurricane Ivan. Science (80-. 309 (5736) https://doi.org/10.1126/science:1112509.
Wang, Zhifeng, Li, Songtao, Hao, Yan, Ma, Yan, Wu, Kejian, 2020. Estimation and Prediction of Typhoons and Wave Overtopping in Qingdao. China. J. Ocean Univ. China 19 (5), 1017–1028. https://doi.org/10.1007/s11802-020-4378-4.
Waseda, T., Hallerstig, M., Ozaki, K., Tomita, H., 2011. Enhanced freak wave occurrence with narrow directional spectrum in the North Sea. Geophys. Res. Lett. 38 (13), n/a–n/a. https://doi.org/10.1029/2011GL047779.
Waseda, T., Kinoshita, T., Tamura, H., 2009. Evolution of a Random Directional Wave and Freak Wave Occurrence. J. Phys. Oceanogr. 39, 621–639. https://doi.org/10.1175/2008JPO4031.1.
Welch, P., 1967. The Use of Fast Fourier Transform for the Estimation of Power Spectra: A Method Based on Time Averaging Over Short, Modified Periodograms. IEEE Trans. Audio Electroacoust. 15 (2), 70–73. https://doi.org/10.1109/TAU.1967.1161901.
World Meteorological Organization, 2018. Guide to Wave Analysis and Forecasting, WMO-No. 702.
Yamaguchi, M., Vitart, F., Lang, S.T.K., Magnusson, L., Elsberry, R.L., Elliott, G., Kyouda, M., Nakazawa, T., 2015. Global Distribution of the Skill of Tropical Cyclone Activity Forecasts on Short- to Medium-Range Time Scales. Weather Forecast. 30, 1695–1709. https://doi.org/10.1175/WAF-D-14-00136.1.
Young, I., 2017. A Review of Parametric Descriptions of Tropical Cyclone Wind-Wave Generation. Atmosphere (Basel). 8, 194. https://doi.org/10.3390/atmos8100194.
Young, I.R., 1988. A PARAMETRIC HURRICANE WAVE PREDICTION MODEL. Coast. Eng. Proc. 1, 82. https://doi.org/10.9753/icce.v21.82.
Yu, Y., Dong, C., Shan, H., Zou, B., 2020. Statistical analysis of intensity variations in tropical cyclones in the East China Sea passing over the Kuroshio. J. Oceanol. Limnol. 38, 1632–1639. doi:10.1007/s00343-019-9069-x.
Zakharov, V.E., 1972. Stability of periodic waves of finite amplitude on the surface of a deep fluid. J. Appl. Mech. Tech. Phys. 9 (2), 190–194. https://doi.org/10.1007/BF00913182.
Zakharov, V.E., Filonenko, N.N., 1967. Energy spectrum for stochastic oscillations of the surface of a liquid. Sov. Phys. Dokl. 11, 881–883.